

## Article

# Preparation and Investigation of Pd and Bimetallic Pd-Sn Nanocrystals on $\gamma$ -Al<sub>2</sub>O<sub>3</sub>

Ivan Bondarchuk <sup>1</sup>, Francisco José Cadete Santos Aires <sup>1,2</sup> , Grigoriy Mamontov <sup>1</sup>  and Irina Kurzina <sup>1,\*</sup> 

<sup>1</sup> National Research Tomsk State University, 36 Lenin Ave., 634050 Tomsk, Russia; ivanich\_91@mail.ru (I.B.); francisco.aires@ircelyon.univ-lyon1.fr (F.J.C.S.A.); grigoriymamontov@mail.ru (G.M.)

<sup>2</sup> IRCELYON CNRS, UMR 5256, Univ Lyon, Université Claude Bernard Lyon 1, 2 Avenue Albert Einstein, CEDEX, 69626 Villeurbanne, France

\* Correspondence: kurzina99@mail.ru

**Abstract:** One of the key factors for producing highly dispersed controlled nanoparticles is the method used for metal deposition. The decomposition of metal-organic precursors is a good method for deposition of metal nanoparticles with very small sizes and narrow size distributions on the surface of various supports. The preparation process of Pd and bimetallic Pd-Sn nanoparticles supported onto  $\gamma$ -Al<sub>2</sub>O<sub>3</sub> is considered. The samples were prepared by diffusional co-impregnation of the  $\gamma$ -Al<sub>2</sub>O<sub>3</sub> support by using organometallic Pd(acac)<sub>2</sub> and Sn(acac)<sub>2</sub>Cl<sub>2</sub> precursors. To achieve the formation of Pd and bimetallic Pd-Sn nanoparticles on the support surface, the synthesized samples were then subjected to thermal decomposition under Ar (to decompose the organometallic bound to the surface while keeping the formed nanoparticles small) followed by an oxidation in O<sub>2</sub> (to eliminate the organic compounds remaining on the surface) and a reduction in H<sub>2</sub> (to reduce the nanoparticles oxidized during the previous step). A combination of methods (ICP-OES, TPR-H<sub>2</sub>, XPS, TEM/EDX) was used to compare the physical-chemical properties of the synthesized Pd and bimetallic Pd-Sn nanoparticles supported on the  $\gamma$ -Al<sub>2</sub>O<sub>3</sub>. The three samples exhibit narrow size distribution with a majority on nanoparticles between 3 and 5 nm. Local EDX measurements clearly showed that the nanoparticles are bimetallic with the expected chemical composition and the measured global composition by ICP-OES. The surface composition and electronic properties of Pd and Sn on the  $\gamma$ -Al<sub>2</sub>O<sub>3</sub> support were investigated by XPS, in particular the chemical state of palladium and tin after each step of thermal decomposition treatments (oxidation, reduction) by the XPS method has been carried out. The reducibility of the prepared bimetallic nanoparticles was measured by hydrogen temperature programmed reduction (TPR-H<sub>2</sub>). The temperature programmed reduction TPR-H<sub>2</sub> experiments have confirmed the existence of strong surface interactions between Pd and Sn, as evidenced by hydrogen spillover of Pd to Sn (Pd-assisted reduction of oxygen precovered Sn). These results lead us to propose a mechanism for the formation of the bimetallic nanoparticles.

**Keywords:** bimetallic nanoparticles; palladium-tin; palladium acetylacetonate; Pd(acac)<sub>2</sub>; tin(IV) bis(acetylacetonate) dichloride; Sn(acac)<sub>2</sub>Cl<sub>2</sub>; mechanism formation of nanoparticles



**Citation:** Bondarchuk, I.; Cadete Santos Aires, F.J.; Mamontov, G.; Kurzina, I. Preparation and Investigation of Pd and Bimetallic Pd-Sn Nanocrystals on  $\gamma$ -Al<sub>2</sub>O<sub>3</sub>. *Crystals* **2021**, *11*, 444. <https://doi.org/10.3390/cryst11040444>

Academic Editor: Jiarui He

Received: 7 February 2021

Accepted: 15 April 2021

Published: 19 April 2021

**Publisher's Note:** MDPI stays neutral with regard to jurisdictional claims in published maps and institutional affiliations.



**Copyright:** © 2021 by the authors. Licensee MDPI, Basel, Switzerland. This article is an open access article distributed under the terms and conditions of the Creative Commons Attribution (CC BY) license (<https://creativecommons.org/licenses/by/4.0/>).

## 1. Introduction

Bimetallic systems have a rather wide range of applications from bio-medicine [1–4] to agriculture [5] through many industrial related domains (optics [3,4,6,7], magnetism [3,7], microelectronics [8], depollution [9–11], energy [11,12], catalysis [4,13–15]). In the field of catalysis [13,15], the addition of a second metal to an already active metal may improve its catalytic performance increasing its activity and/or selectivity allowing thus allowing to work at lower temperatures and to form as a small amount as possible of unwanted products. Formation of a bimetallic may also give the possibility of modulating the activity (indeed a very active phase may lead to strong deactivation) and the selectivity thus being able to change the orientation of the products of a selective reaction following the needs.

Furthermore, it can also provide better stability of the active phase and better resistance to poisoning. Finally, if we add to the previous points the possibility of diluting the active sites of, often, expensive metals with low-cost metals we have a set of factors that will lead to lower costs of operation and materials.

It is expected that the properties of bimetallic particles correspond to not only to a combination of the properties of both metals but that synergy between them will result in unique chemical and physical new properties. The second metal can strongly modulate the properties of the first metal by decorating specific sites at the surface [16–18], by stabilizing the initial catalyst in preventing poisoning [19], by diluting the initial sites at the surface yielding specific atomic ensembles [20,21] with unique controlled properties or by electronic interaction yielding modified electronic structures with a strong influence on reactive gas molecules adsorption and/or dissociation [22,23].

Pd supported catalysts are successfully used in a variety of very different reactions such as the low-temperature butadiene hydrogenation both in liquid [24] and gas phases [25,26], the rather high temperature reaction of methane total oxidation [27–29], three-way catalysis [30] reduction reactions [31] or cross-coupling reactions [32] such as the well known Suzuki-Miyaura reaction [33]. Development of Pd-based bimetallic supported catalysts have thus found an immense success amid the catalysis community since they allow the tuning and refinement of the already remarkable catalytic properties of pure Pd [9,12,20,21]; for instance, to stabilize the catalyst in presence of poisons [19] or to improve its selectivity [34]. In these systems, large effects are observed for bimetallic surfaces that combine a metal with an electron-rich *d*-band (late transition metal) and a metal with an electron-poor valence band (early-transition or *sp* metal). It is thus interesting to consider tin; its role in these systems is usually connected (correlated) with the modification of Pd *d*-band and consequently related with particle adsorption properties. X-ray photoelectron spectroscopy (XPS) investigation of Pd-Sn alloy indicated a strong bimetallic interaction resulting in a noble metal-like electronic structure [35–38]. Therefore, a great effort has been made to investigate bimetallic systems based on palladium and tin in order to prepare novel catalysts for various applications [34–58]. Due to the highly propensity of tin to oxidize during oxidation reactions a particular interest was taken to the interaction between palladium and tin oxide species [39–41]. Strong mutual interaction leads, for example, to the formation of mixed oxides Pd-Sn-O that exhibit specific properties when compared to SnO<sub>2</sub> and PdO. These highly active sites at the metal/oxide interface can be responsible for particular metal-substrate interactions occurring at the particle periphery i.e., at the metal-oxide boundary [40,41].

The synthesis of mono and bimetallic nanoparticles can be performed by different (physical and chemical) methods [59–61] which have their advantages and their flaws. Cluster-beam deposition in vacuum allows a rather good control of the nanoparticles size and, above all, of their chemical composition [62,63]; although it has been successfully used for deposition on powder supports [19,64] it remains cumbersome and almost useless to obtain provide amounts of catalysts. These drawbacks can be solved by using cluster-beam deposition in liquids but, in this case, size distributions tend to be rather broad [65]. Flame spray method can provide direct synthesis of both (bi)metallic and support phases [66]; however, it is very sensitive to the experimental parameters and is prone to oxidation and coking. Methods such as oxidative etching can give rather good control of nanoparticle shape [67] and the use of di-block copolymer inverse micelle templates yield well organized nanoparticles rather well controlled in size and composition [68]. These two latter methods are, however, not very well adapted to small (<5 nm) nanoparticles. However, among all methods, chemical impregnation of powder supports with metallic precursors is certainly the most used one to obtain supported (bi)metallic catalysts. As such, they have been extensively used to obtain PdSn catalysts either by using inorganic tin precursor such as stannic chloride or stannous chloride and palladium chloride or nitrate [42–52] or organic precursors such as acetylacetonates [53–58] which result from the association of acetylacetonate, one of the most commonly used organic oxygen ligands with donor atoms, with Pd(II) yielding a very stable chelate complex Pd(acac)<sub>2</sub>. The main advantage of the former is the

simplicity associated to (at least for most of them) their solubility in water. Post-treatments (decomposition, calcination, reduction) of the catalysts may however need the use of temperatures (above 450 °C) sufficiently high to remove any remaining Cl or N species that may be noxious for their catalytic behavior. The latter certainly has the drawback of not being soluble in water and thus need the use of organic solvents; nevertheless, it yields rather controlled (size/composition) supported nanoparticles. Palladium complex Pd(acac)<sub>2</sub> is thus a widely used palladium precursor due to the potential possibility of a higher dispersion of the obtained nanoparticles in comparison to inorganic metal systems. Therefore, the structural features of the precursor could play an important role. The ability of many metals to form thermally stable volatile chelate compounds with β-diketonates makes it possible to use acetylacetonate complexes to form bimetallic nanoparticles on the surface of the oxide supports. The formation of supported catalysts using organic precursors originates in the early work of Yermakov [69,70]. As pointed out above, the post-impregnation treatment is crucial to obtain well controlled (size/composition) nanoparticles. Initially, Yermakov and Kuznetsov suggested that a high temperature treatment under hydrogen would be enough to decompose and eliminate the organic species yielding a supported monometallic catalyst [70]; later Berdala et al. [71] found that a calcination, prior to the reduction step, help not only to better eliminate the organic species but also resulted in better dispersions. It was in the 1990's that Renouprez et al. [72–75] in Lyon initiated a series of studies aimed at extending this method to the synthesis of various Pd-based bimetallic catalysts. In particular, the study of the PdCu [73] system clearly showed that a step of decomposition under inert gas prior to calcination and reduction clearly ameliorate not only the dispersion of the nanoparticles but also their homogeneity in composition. This observation resulted in the use of this protocol for the studies of PdMn [74] and PdPt [75] with clear success that was more recently extended to the PdSn system [34]. Unlike the other systems [72–75], where the two metallic acetylacetonates involved in the synthesis are bis-acetylacetonates (Pd(Acac)<sub>2</sub> and M(Acac)<sub>2</sub>; M = Ni, Cu, Mn, Pt) which are supposed to adsorb in a planar configuration on the oxide support, the tin precursor is a di-chloride stabilized bis-acetylacetonate ([Sn(acac)<sub>2</sub>]Cl<sub>2</sub>) [34] which may affect the adsorption of the molecule on the alumina and may have consequences on the interaction between adsorbed species. Indeed, the number of metal ions, the internuclear distance between metal ions and the geometric arrangement of metal ions in the complex are determined by the choice of metal complex for the impregnation. The spacing between metal ions on the support surface is regulated by the overall size of the complex and can be varied by changing the size of the organic ligands without changing the arrangement of the metal ions. The ability to create a uniform surface is one advantage of the designed dispersion approach which can be exploited to determine the relationships between properties and the structure of the supported nanoparticles. This feature becomes important when one attempts to stabilize the metal ions for the formation of bimetallic phases [72–76]. This approach can be used in both real systems and well-defined model systems studied to understand elementary processes on the surfaces. This structural and chemical information is correlated with the physical-chemical properties for the various applications. A correlation between the physicochemical properties and the adsorption behavior can be obtained by associating straightforward but consistent and complementary different characterization techniques. The purpose of the study here presented is to take advantage of the use of such techniques (ICP-OES, TPR-H<sub>2</sub>, XPS, TEM/EDX), in conjunction with the post-impregnation treatment protocol, to gain insight on the path leading to the formation of the supported nanocrystals with rather uniform sizes (although avoiding almost atomic dispersion as can be obtained from the use of metal tetraammine precursors [77], for instance) that, eventually, will help us to devise how to better control of their physico-chemical characteristics.

## 2. Results and Discussion

Elemental composition, surface morphology, electronic state and redox properties of Pd-Sn bimetallic nanoparticles supported on γ-Al<sub>2</sub>O<sub>3</sub>.

The results of the chemical analysis obtained by ICP-OES are given in Table 1. The metallic content (Pd wt% or (Pd + Sn) wt%) is around 1.3–1.4 wt% for the three samples. This value is slightly higher than the expected one (1.2 wt%) while the Pd/Sn atomic ratio is slightly lower than expected one but within an acceptable margin of less than 10% (cf. Table 3 in the Materials and Methods section).

**Table 1.** Pd and Sn content according to ICP-OES (wt%) and corresponding (at%) content, and average nanoparticle diameter corresponding to the histograms in Figure obtained from TEM measurements.

Name Sample	Precalculated Pd/Sn (at)	Measured Pd (wt%)	Pd (at%)	Measured Sn (wt%)	Sn (at%)	Pd/Sn (at)	Average Size, nm
Pd/ $\gamma$ -Al <sub>2</sub> O <sub>3</sub>	—	1.32	1.27	—	—	—	3.5
3Pd1Sn/ $\gamma$ -Al <sub>2</sub> O <sub>3</sub>	3:1	0.96	0.93	0.39	0.33	2.82	3.2
1Pd1Sn/ $\gamma$ -Al <sub>2</sub> O <sub>3</sub>	1:1	0.64	0.62	0.74	0.64	0.97	2.8

TEM observation (Figure 1), after the last preparation step (reduction at 500 °C during 2 h), of the three samples reveals that the metal is well dispersed over the support in the form of small nanoparticles (Figure 1a,d,g). Relevant histograms presented in Figure 2 show rather narrow size distributions (1 to 6 nm with a large majority of the nanoparticles around 2 to 4 nm). The average diameter of the nanoparticles slightly decreases when the Pd content of the nanoparticles also decreases (see Table 1): from 3.5 nm for pure Pd/ $\gamma$ -Al<sub>2</sub>O<sub>3</sub> to 2.8 nm for the sample 1Pd1Sn/ $\gamma$ -Al<sub>2</sub>O<sub>3</sub>. In order to determine the local composition of the nanoparticles we have performed EDX (Energy Dispersive X-ray spectroscopy) over small collections of (5–10) nanoparticles. The results presented in Figure 3a show that, for both PdSn samples, the nanoparticles are bimetallic and that the composition is close to the desired one ( $75 \pm 10\%$  for 3Pd1Sn/ $\gamma$ -Al<sub>2</sub>O<sub>3</sub> and  $50 \pm 10\%$  for 1Pd1Sn/ $\gamma$ -Al<sub>2</sub>O<sub>3</sub>). Furthermore, we could make a very few EDX measurements on rather large nanoparticles (4–5 nm) within reasonable acquisition times and without compromising their stability under the focussed electron beam. The results shown in Figure 3b for three nanoparticles for each sample clearly reveal that these individual nanoparticles are bimetallic and establish the validity of the local EDX measurements performed over small collections of (5–10) nanoparticles to show that a very large majority (if not all) of the nanoparticles are bimetallic and consistent with global ICP-OES results.

HRTEM imaging of individual nanoparticles reveal that they are crystalline (sometimes twinned in the case of pure Pd) and also helped confirm the bimetallic character of the nanoparticles for the PdSn samples, in particular for 1Pd1Sn/ $\gamma$ -Al<sub>2</sub>O<sub>3</sub>. For the sample Pd/ $\gamma$ -Al<sub>2</sub>O<sub>3</sub> the HRTEM images are presented in Figure 1b,c. Both images confirm the Pd *fcc Fm-3m* structure (PDF: 00-046-1043) with a lattice parameter  $a = 0.3890$  nm. Nanoparticle in Figure 1b is observed along a type  $\langle -1\ 1\ 0 \rangle$  direction and the basic planes are of  $\{1\ 1\ 1\}$  and  $\{1\ 0\ 0\}$  types. We have thus arbitrarily chosen the Pd $[-1\ 1\ 0]$  direction to index the visible interplanar distances which are  $d_{(1\ 1\ 1)}$  ( $0.223 \pm 0.05$  nm) and  $d_{(1\ 1\ -1)}$  ( $0.228 \pm 0.05$  nm), separated by  $70.5 \pm 0.5^\circ$ ; and  $d_{(0\ 0\ -2)}$  ( $0.197 \pm 0.05$  nm) separated by  $55.1 \pm 0.5^\circ$  from  $d_{(1\ 1\ -1)}$ . Indeed, for this structure there is an extinction for interplanar distances like  $d_{(0\ 0\ -1)}$  and only  $d_{(0\ 0\ -2)}$  interplanar distances are visible. The measured interplanar distances and angles clearly correspond to the expected ones (PDF: 00-046-1043) within the measurement precision:  $0.2246$  nm for  $d_{(1\ 1\ 1)}$  and  $d_{(1\ 1\ -1)}$ , separated by  $70.53^\circ$  and  $0.1945$  nm for  $d_{(0\ 0\ -2)}$  separated by  $54.74^\circ$  from  $d_{(1\ 1\ -1)}$ . The nanoparticle in Figure 1c is viewed along a type  $\langle 0\ 0\ 1 \rangle$  direction with basic planes of the  $\{1\ 0\ 0\}$  and  $\{0\ 1\ 0\}$  types. We have thus chosen the Pd $[0\ 0\ 1]$  direction with visible interplanar distances  $d_{(2\ 0\ 0)}$  ( $0.191 \pm 0.05$  nm) and  $d_{(0\ 2\ 0)}$  ( $0.197 \pm 0.05$  nm) separated by  $89.6 \pm 0.5^\circ$ . Here again interplanar distances and angle are, within the measurement precision, in agreement with the expected ones:  $0.1945$  nm for  $d_{(2\ 0\ 0)}$  and  $d_{(0\ 2\ 0)}$  separated by  $90^\circ$ .

In the case of the two bimetallic samples, we have only observed nanoparticle orientations (and thus basic interplanar distances and angles) consistent with cubic structures. Therefore, in the case of the 3Pd1Sn/ $\gamma$ -Al<sub>2</sub>O<sub>3</sub> sample, we dismissed the pro-

posed orthorhombic (PDF: 00-041-1409) and tetragonal (PDF: 03-065-9510) structures to retain the also proposed *bcc Pm-3m* structure (PDF: 03-065-8225) with a lattice parameter  $a = 0.3967$  nm. We must mention that this sample, surprisingly and inexplicably, yield the poorest high-resolution image quality of the three samples.

HRTEM images of nanoparticles from  $3\text{Pd}1\text{Sn}/\gamma\text{-Al}_2\text{O}_3$  are presented in Figure 1e,f. Both nanoparticles are oriented in a  $\langle 1\ 1\ 0 \rangle$  type direction. As previously, we have arbitrarily chosen the  $\text{Pd}_3\text{Sn}$   $[-1\ 1\ 0]$  giving rise to visible interplanar distances  $d_{(0\ 0\ -2)}$  and  $d_{(-1\ -1\ -1)}$ ; the third interplanar distance was either absent or very faint to provide a proper measurement. The measurements of the nanoparticle in Figure 1e show  $d_{(0\ 0\ -2)}$  ( $0.203 \pm 0.05$  nm) and  $d_{(-1\ -1\ -1)}$  ( $0.231 \pm 0.05$  nm) separated by a  $54.3 \pm 0.5^\circ$  angle. For the nanoparticle in Figure 1f, we have measured  $d_{(0\ 0\ -2)}$  ( $0.201 \pm 0.05$  nm) and  $d_{(-1\ -1\ -1)}$  ( $0.232 \pm 0.05$  nm) separated by a  $54.5 \pm 0.5^\circ$  angle. These numerical values correspond to the expected ones for  $\text{Pd}_3\text{Sn}$  (PDF: PDF: 03-065-8225;  $d_{(0\ 0\ -2)}$  (0.1984 nm) and  $d_{(-1\ -1\ -1)}$  (0.2290 nm) separated by a  $57.74^\circ$  angle) within the precision of the measure. However, it is difficult to state that these results confirm that the nanoparticles are bimetallic since, for the observed orientations the interplanar distances for *fcc* Pd and for *bcc*  $\text{Pd}_3\text{Sn}$  are equivalent and very close if we take into account the precision of the measure.

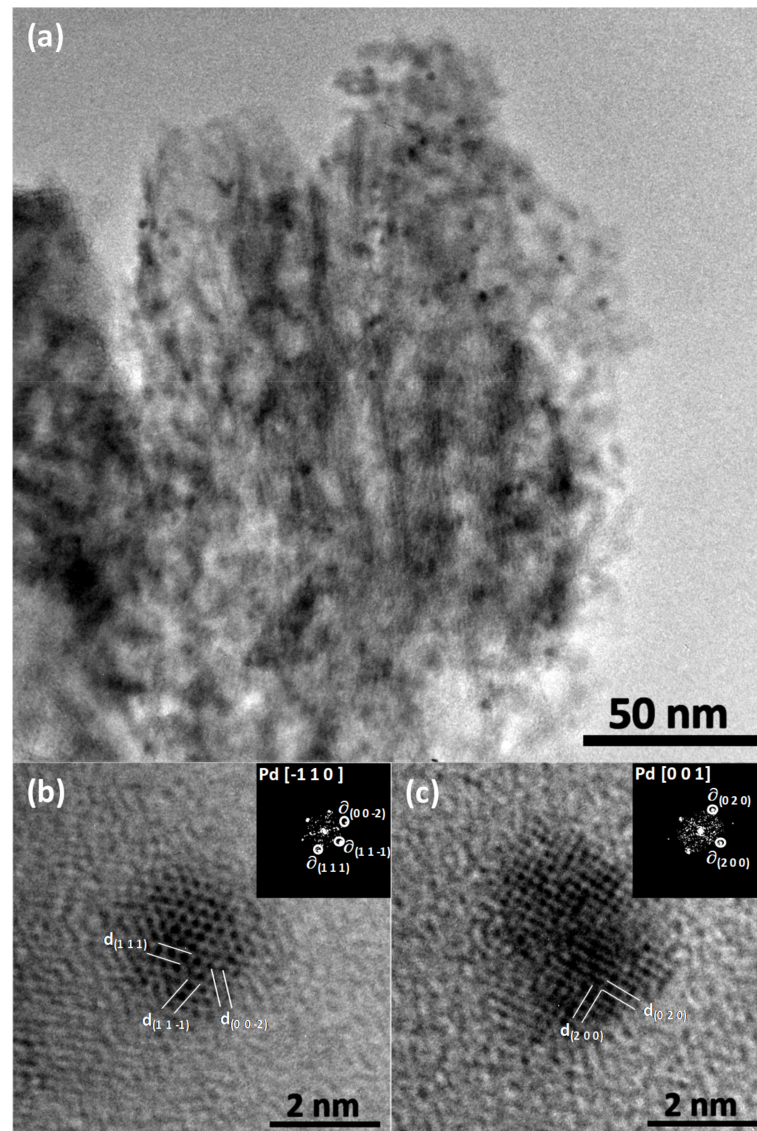


Figure 1. Cont.

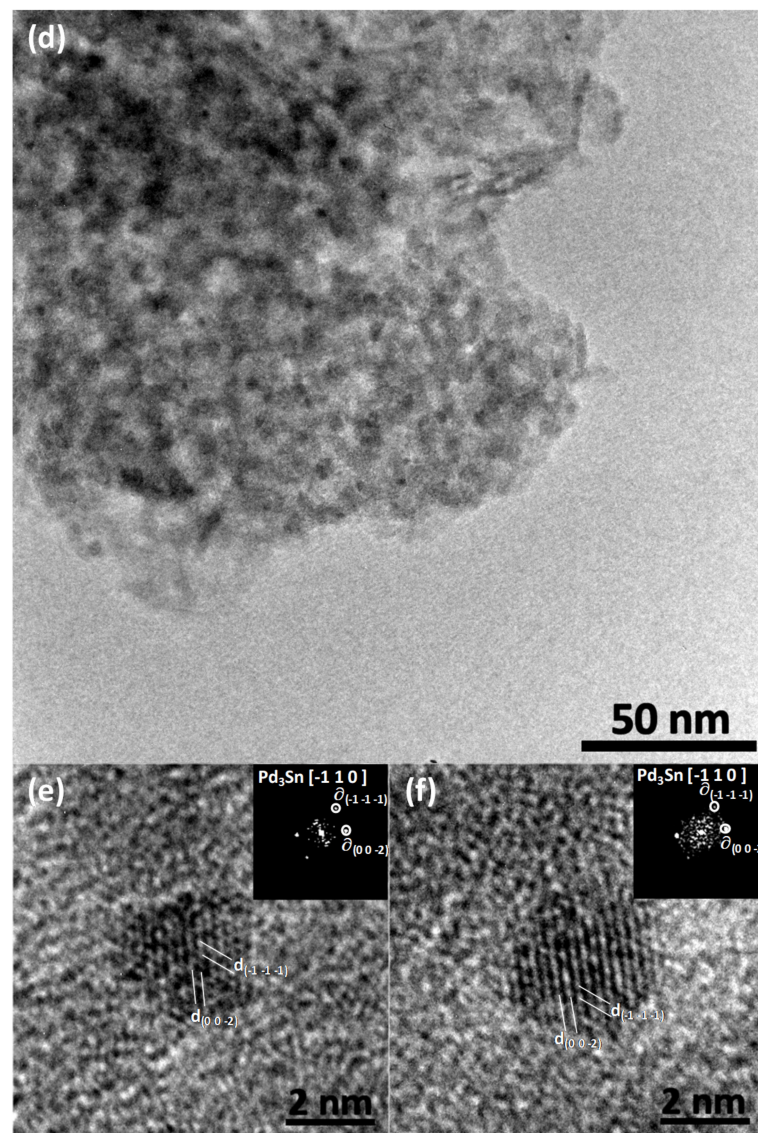
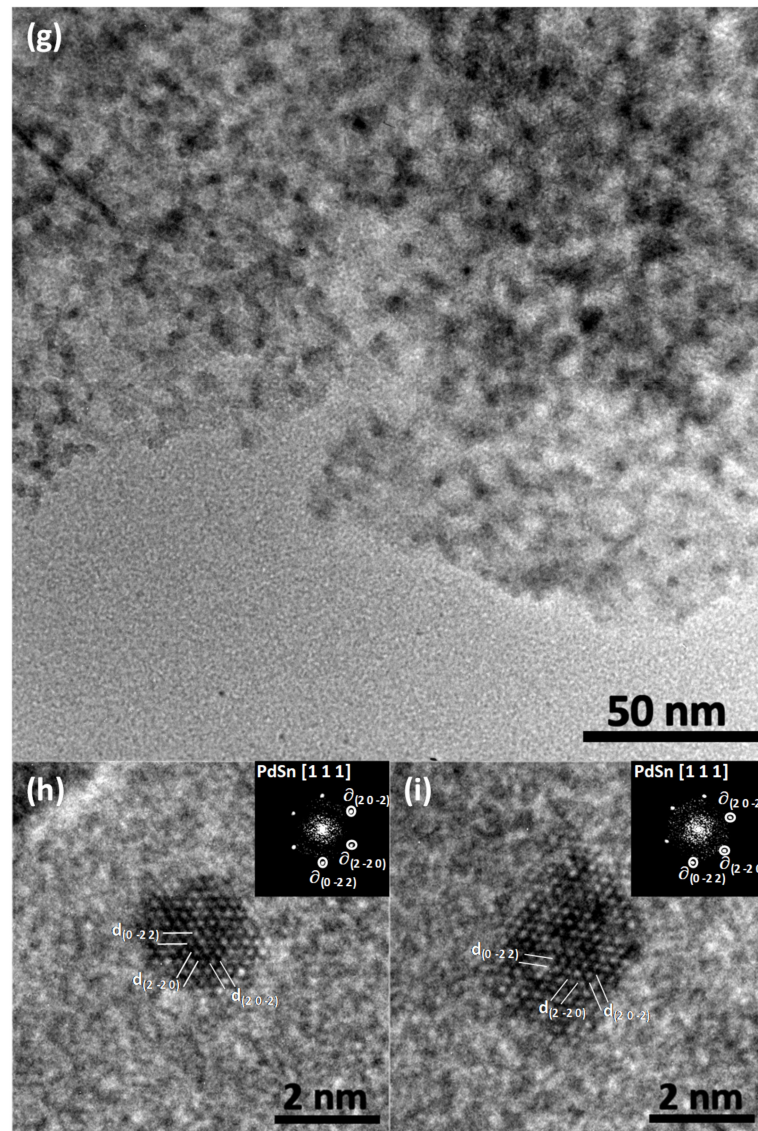


Figure 1. Cont.



**Figure 1.** TEM (a,d,g) and HRTEM (b,c,e,f,h,i) images of the samples Pd/ $\gamma$ -Al<sub>2</sub>O<sub>3</sub> (a–c); 3Pd1Sn/ $\gamma$ -Al<sub>2</sub>O<sub>3</sub> (d–f) and 1Pd1Sn/ $\gamma$ -Al<sub>2</sub>O<sub>3</sub> (g–i). Inserts in the HRTEM images correspond to the 2D-FFTs of the respective nanoparticles; in the inserts  $\vartheta_{(hkl)}$  correspond to  $1/d_{(hkl)}$ .

Finally, for sample 1Pd1Sn/ $\gamma$ -Al<sub>2</sub>O<sub>3</sub>, we noticed that for both nanoparticles presented in Figure 1h,i, we had three similar interplanar distances separated  $\approx 60^\circ$  angles. This is possible either for the [1] orientation in *hcp* structures or for the [1 1 1] orientation in *fcc* structures. We have thus dismissed the proposed orthorhombic structure (PDF: 00-004-0803). With no other possibility to our knowledge in literature, we have thus decided to use a *fcc* structure with a lattice parameter  $a = 0.519$  nm derived from the Vegard law for a PdSn stoichiometry (experimentally confirmed by EDX) based on the linear combination of parameters of Pd *fcc Fm-3m* (PDF: 00-046-1043;  $a = 0.3890$  nm) and  $\alpha$ -Sn *fcc* diamond-like (PDF: 01-086-2266;  $a = 0.6489$  nm) structures. We have thus two nanoparticles oriented in the [1 1 1] direction with visible interplanar distances  $d_{(0-2-2)}$ ,  $d_{(2-2-0)}$  and  $d_{(2-0-2)}$ . For nanoparticle in Figure 1h we have  $d_{(0-2-2)}$  ( $0.184 \pm 0.05$  nm),  $d_{(2-2-0)}$  ( $0.185 \pm 0.05$  nm) and  $d_{(2-0-2)}$  ( $0.184 \pm 0.05$  nm), separated, respectively, by  $60.4 \pm 0.5^\circ$  and  $59.8 \pm 0.5^\circ$ . For the nanoparticle in Figure 1i we obtained  $d_{(0-2-2)}$  ( $0.185 \pm 0.05$  nm),  $d_{(2-2-0)}$  ( $0.186 \pm 0.05$  nm) and  $d_{(2-0-2)}$  ( $0.181 \pm 0.05$  nm), separated, respectively, by  $59.9 \pm 0.5^\circ$  and  $60.2 \pm 0.5^\circ$ . This is in excellent agreement with the expected value ( $0.184$  nm) for  $d_{(0-2-2)}$ ,  $d_{(2-2-0)}$  and  $d_{(2-0-2)}$ , which are separated by  $60^\circ$  angles. This confirms thus that our assumption to

use a *fcc* structure for PdSn based on the Vegard law and *fcc* Pd and Sn is an appropriate solution, despite lacking formal evidence. This also confirms, if needed, the EDX results showing that the nanoparticles are bimetallic.

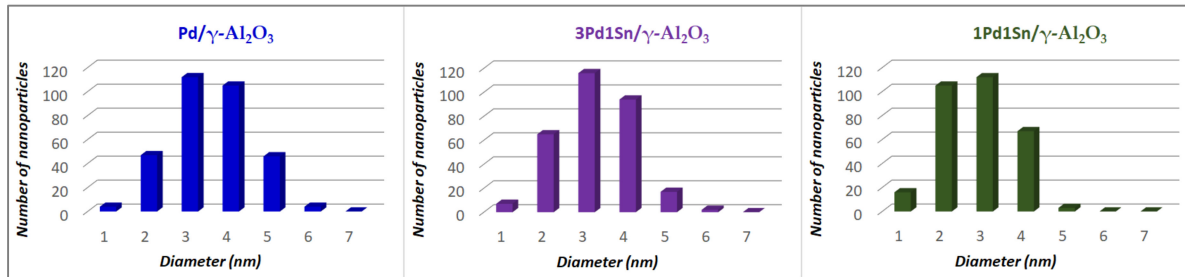


**Figure 2.** Nanoparticle size histograms for Pd/ $\gamma$ -Al<sub>2</sub>O<sub>3</sub> (blue, left); 3Pd1Sn/ $\gamma$ -Al<sub>2</sub>O<sub>3</sub> (violet, center) and 1Pd1Sn/ $\gamma$ -Al<sub>2</sub>O<sub>3</sub> (green, right).

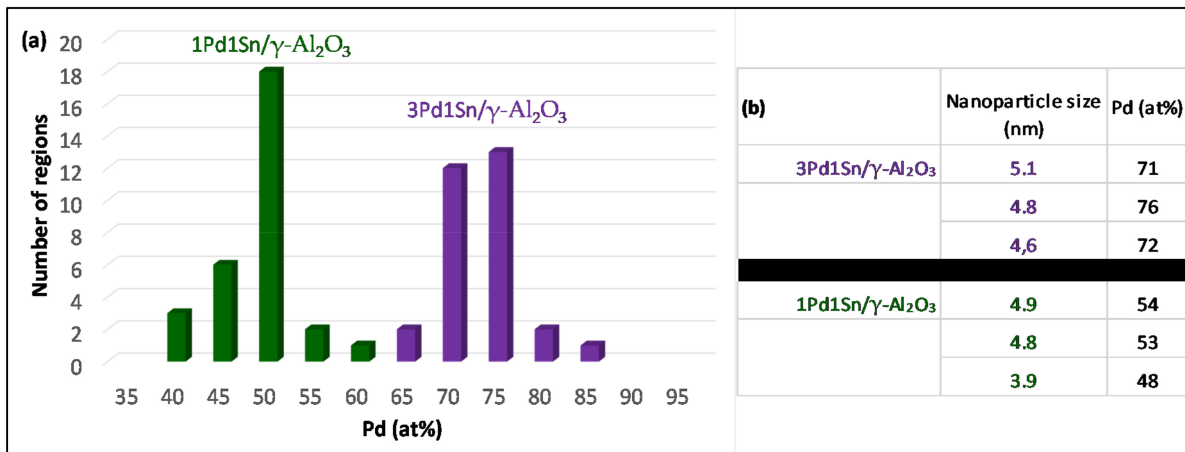


**Figure 3.** (a) Pd content (at%; Sn content is the complement to 100%) measured by EDX (on regions of 5–10 nanoparticles for 3Pd1Sn/ $\gamma$ -Al<sub>2</sub>O<sub>3</sub> (violet) and 1Pd1Sn/ $\gamma$ -Al<sub>2</sub>O<sub>3</sub> (green). (b) Pd content (at%) measured by EDX on few large (size is given) individual nanoparticles for 3Pd1Sn/ $\gamma$ -Al<sub>2</sub>O<sub>3</sub> and 1Pd1Sn/ $\gamma$ -Al<sub>2</sub>O<sub>3</sub>.

The surface composition and electronic properties of Pd and Sn within the three samples supported on  $\gamma$ -Al<sub>2</sub>O<sub>3</sub> were investigated by XPS. The XPS spectra for Pd3d<sub>5/2</sub> of all the samples after reduction at 500 °C in hydrogen for 2 h are shown in Figure 4. For all samples, the binding energy of Pd3d<sub>5/2</sub> is in the range of 334.7–335.2 eV, indicating the presence of metallic palladium species [78,79]. For Pd/ $\gamma$ -Al<sub>2</sub>O<sub>3</sub> and 3Pd1Sn/ $\gamma$ -Al<sub>2</sub>O<sub>3</sub> (a sample where the nanoparticles are supposed to be Pd-rich) the binding energies of Pd3d<sub>5/2</sub> were similar (335.2 eV), indicating that both the phase of  $\gamma$ -Al<sub>2</sub>O<sub>3</sub> and the size had no significant influence on the electronic properties of the metallic Pd-containing particles [34]. However, the binding energy of Pd3d<sub>5/2</sub> for 1Pd1Sn on  $\gamma$ -Al<sub>2</sub>O<sub>3</sub> is shifted towards a smaller value (334.7 eV) indicating that Sn addition modifies the electronic properties of Pd in this sample where nanoparticles are, contrary to 3Pd1Sn/ $\gamma$ -Al<sub>2</sub>O<sub>3</sub> no longer Pd-rich [39]. A minor contribution of unreduced Pd (oxide) is also observed (BE  $\approx$  336.3–336.4 eV); this can be due to uncomplete reduction, as it is certainly the case for Pd/ $\gamma$ -Al<sub>2</sub>O<sub>3</sub> and/or to the presence of tin for the bimetallic samples (this is addressed later in the text).

The deconvoluted XPS spectra of Sn3d<sub>5/2</sub> core-level for 3Pd1Sn/ $\gamma$ -Al<sub>2</sub>O<sub>3</sub> and 1Pd1Sn/ $\gamma$ -Al<sub>2</sub>O<sub>3</sub> are shown in Figure 5 and the (semi-)quantitative data extracted from these spectra are presented in Table 2. Both bimetallic samples demonstrate two similar components of tin species. The higher binding energy (487.0–487.2 eV) can be related to tin oxide remaining even if the samples were reduced in hydrogen flow at 500 °C for 2 h. This is often the case due to (very) small unavoidable amounts of oxygen dead volume present in the vacuum

locks during sample transfer and to the high propensity of Sn to oxidize. The higher binding energy (487.0–487.2 eV) can be related to tin oxide remaining even if the samples were reduced in hydrogen flow at 500 °C for 2 h. This observation together with the fact that part of tin is reduced simultaneously with palladium by TPR-H<sub>2</sub> suggests, as will be shown below, that the remaining unreduced tin is within the bimetallic nanoparticles. On the other hand, the remaining portion of tin component observed at the lower binding energy in the range 485.1–485.3 eV can be assigned to the presence of palladium-tin alloy [80]. It can be seen also that with the addition of tin the amount of palladium (II) oxide increases for bimetallic Pd-Sn samples.

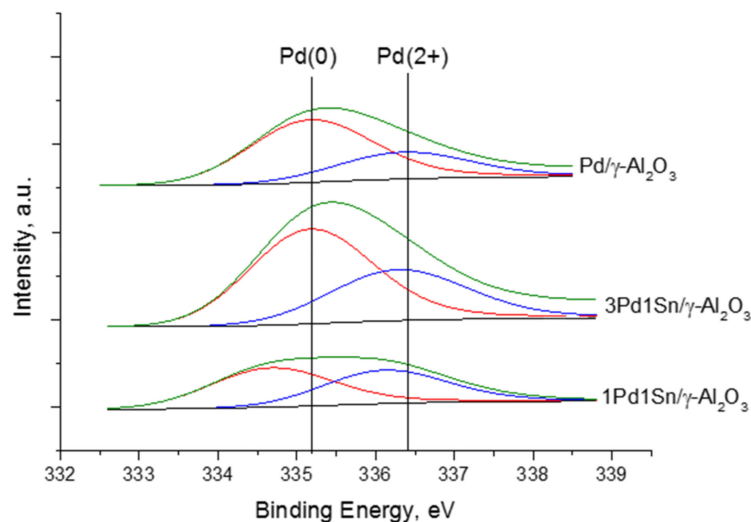


**Figure 4.** Pd3d<sub>5/2</sub> core-level XPS spectra for Pd/γ-Al<sub>2</sub>O<sub>3</sub>, 3Pd1Sn/γ-Al<sub>2</sub>O<sub>3</sub> and 1Pd1Sn/γ-Al<sub>2</sub>O<sub>3</sub>. Deconvolution with two contributions Pd(0) and Pd(2+) is proposed.

Surface composition quantification and binding energy for all synthesized samples are given in Table 2. Surface analysis by XPS showed after deposition one part of the supported Pd(acac)<sub>2</sub> forms PdO species, the other part formed Pd(0) species. Formation of PdO can be attributed to strong interaction of metal precursor Pd(acac)<sub>2</sub> with the γ-Al<sub>2</sub>O<sub>3</sub> surface. Thermal decomposition under Ar inert environment and the successive oxidation-reduction treatments conduce to an increase Pd(0) amount due to the decomposition of acetylacetonate precursors and PdO reduction. The XPS results show that in bimetallic Pd-Sn samples there are two types of tin species, corresponding to Sn(0) species and to oxidized SnO<sub>x</sub> species. We cannot rule out the possibility of a composite Pd-Sn-O phase. It is necessary to notice that the addition of Sn induces an increase of PdO in the obtained Pd-Sn bimetallic nanoparticles. It may be assumed that the addition of Sn during the Pd-Sn bimetallic nanoparticles synthesis, supported onto γ-Al<sub>2</sub>O<sub>3</sub>, leads to a competitive reduction reaction of SnO<sub>x</sub> together with an inhibition of the PdO reduction.

The change in the relative intensity ratios of Pd(0)/Pd(II) and Sn(0)/Sn(IV) with respect to the molar ratios of Pd / Sn in Pd, Sn NPs and bimetallic Pd<sub>x</sub>Sn nanoparticles is also clearly seen from the XPS data. The Pd(0)/Pd(II) ratio in Pd/γ-Al<sub>2</sub>O<sub>3</sub> is approximately 2:1. However, it gradually decreases when the Pd content, in the 3Pd1Sn/γ-Al<sub>2</sub>O<sub>3</sub>, while Pd(0) was minimal in 1Pd1Sn/γ-Al<sub>2</sub>O<sub>3</sub> with the lowest Pd(0)/Pd(II) ratio of approximately 1:1. As can be seen from the data on the elemental composition (Table 1), the amount of palladium in terms of metal is gradually decreasing. On the contrary, the Sn(0)/Sn(IV) ratios decrease monotonically with decreasing Pd/Sn molar ratios. It is known that the noble metal Pd has a relatively high electron negativity and low affinity for oxygen, while Sn is considered an oxophilic metal. The proportions of Pd(0) and Sn(0) with a low oxidation state are relatively higher when Pd dominates. When more Sn is present, a significant amount of SnO<sub>2</sub> is formed on the surface, which in turn prevents the oxidation of Pd, which again leads to an increase in the Pd(0)/Pd(II) ratio. Thus, a distinct affinity for

Pd and Sn towards oxygen is observed. It is also clear that there is a strong segregation of Sn for both bimetallic samples (Table 2).

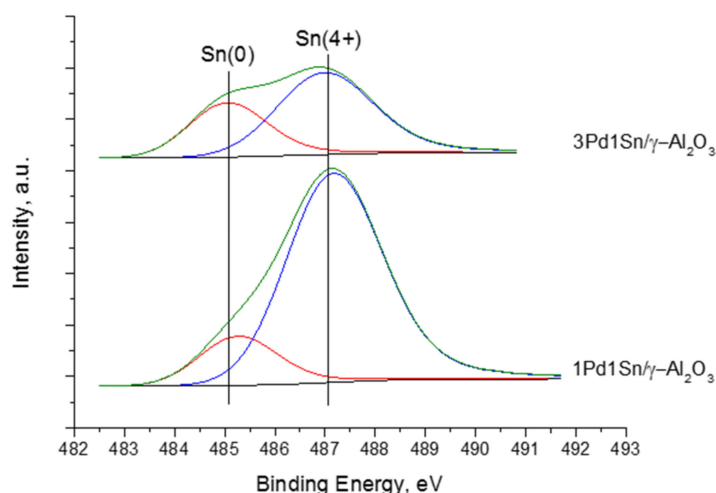


**Figure 5.** Sn3d<sub>5/2</sub> core-level XPS spectra for 3Pd1Sn/γ-Al<sub>2</sub>O<sub>3</sub> and 1Pd1Sn/γ-Al<sub>2</sub>O<sub>3</sub> samples. Deconvolution with two contributions Sn(0) and Sn(4+) is proposed.

**Table 2.** Surface analysis and binding energy for all synthesized samples by XPS.

Name of Sample	Atomic Ratio Pd/Sn	Quantification, at%			Binding Energy, eV		
		Pd	Sn	Pd3d <sub>5/2</sub> (Pd)	Pd3d <sub>5/2</sub> (PdO)	Sn3d <sub>5/2</sub> (Sn)	Sn3d <sub>5/2</sub> (SnO <sub>x</sub> )
Pd/γ-Al <sub>2</sub> O <sub>3</sub>	—	0.08	—	335.2	336.4	—	—
3Pd1Sn/γ-Al <sub>2</sub> O <sub>3</sub>	3:1	0.15	0.11	335.2	336.3	485.1	487.0
1Pd1Sn/γ-Al <sub>2</sub> O <sub>3</sub>	1:1	0.10	0.25	334.7	336.2	485.3	487.2

The obtained TPR-H<sub>2</sub> profiles are shown in Figure 6. All three samples showed TPR profiles with one main reduction peak, which can be attributed to the reduction of PdO to Pd [43]. The monometallic Pd /γ-Al<sub>2</sub>O<sub>3</sub> sample was reduced at 41 °C, while the reduction peak for both bimetallic Pd-Sn samples shifts slightly to 50 °C. It is assumed that the finer particles of Pd and both Pd-Sn samples obtained from acetylacetonate precursors in toluene led to a stronger interaction with the γ-Al<sub>2</sub>O<sub>3</sub> support. The large negative peak of the monometallic Pd sample at 97 °C can be attributed to the decomposition of Pd-β-hydride, which agrees with the literature data [43]. The negative peak associated with the decomposition of the Pd-β-hydride phase demonstrates that some Pd particles form the Pd β-hydride phase at the initial stage of the reduction at low temperatures.

Notably, the monometallic Pd/γ-Al<sub>2</sub>O<sub>3</sub> sample shows extended small reduction peaks in the temperature range 200–400 °C, which may be associated with the reduction of stronger bound palladium nanoparticles [81]. TPR-H<sub>2</sub> profiles of the bimetallic Pd-Sn samples show different behavior in comparison with monometallic Pd sample. In particular, the bimetallic Pd-Sn samples do not show a peak associated with the decomposition of the Pd-β-hydride phase, which means that the presence of Sn limits the formation of the Pd-β-hydride phase. On the contrary, instead, a positive peak is observed in the temperature range 60–200 °C, but without the decomposition peak of the Pd-β-hydride phase. Most likely, the reduction process in this temperature range can be complex, which can indicate either the presence of two mixed phases, or two closely spaced separate stages of the reduction of the states of palladium and tin [82]. It can be noted that, in the case of bimetallic Pd-Sn samples, the TCD signal intensity significantly decreases with an increase of the Sn content (or a decrease of the Pd content). It is noteworthy, the TPR profiles of bimetallic Pd-Sn samples demonstrate reduction in the temperature range at

60–200 °C, which is absent in the TPR-H<sub>2</sub> profile of the monometallic Pd sample. Most likely, this feature is associated with the addition of Sn. When Sn is added to Pd, the intensity of the TCD signal in the temperature range at 60–200 °C decreases sharply and is accompanied by the appearance of a positive reduction band in the TPR profiles of bimetallic Pd-Sn samples at temperatures below 200 °C. This may indicate the reduction of bimetallic Pd-Sn particles [80].

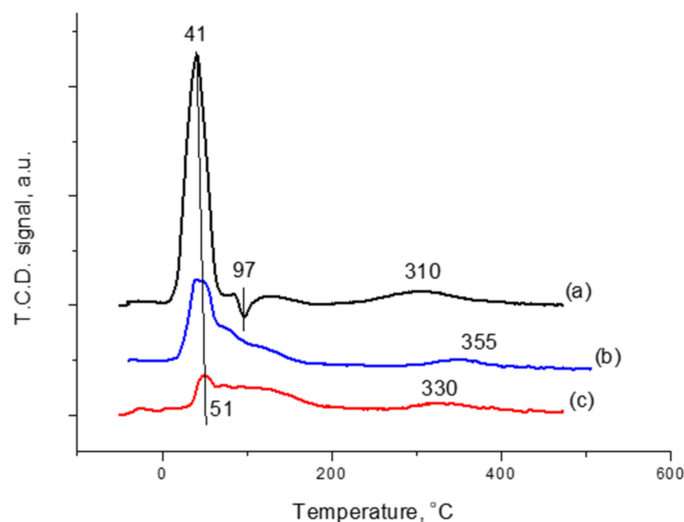


**Figure 6.** TPR profiles of synthesized samples: (a) Pd/ $\gamma$ -Al<sub>2</sub>O<sub>3</sub>, (b) 3Pd1Sn/ $\gamma$ -Al<sub>2</sub>O<sub>3</sub> and (c) 1Pd1Sn/ $\gamma$ -Al<sub>2</sub>O<sub>3</sub>.

This correlates with a decrease of the signal intensity of Pd- $\beta$ -hydride, which may indicate that some of the oxidized states of Pd are no longer available for the formation of Pd- $\beta$ -hydride. Presumably, the indicated feature of reduction at temperatures of 60–200 °C, which is present only in bimetallic Pd-Sn samples, can probably be associated with the presence of mixed states, assumedly by the phase of the Pd-Sn alloy. This may indicate that the presence of Sn inhibits the formation of the Pd- $\beta$ -hydride phase or that Pd is present in another form, such as a Pd-Sn alloy, which prevents the formation of the  $\beta$ -palladium hydride phase [53]. It can be noted that in the TPR-H<sub>2</sub> profiles of bimetallic Pd-Sn samples, which show features of reduction at temperatures of 60–200 °C, there is a decrease in the reduction temperature for Sn particles, the volume reduction of which occurs at temperatures of 450 °C and above [83]. The reduction features present in the temperature range of 300–400 °C can be attributed to the reduction of small surface Sn particles [84]. An obvious feature of TPR-H<sub>2</sub> profiles containing both Sn and Pd is the smaller area of the Sn reduction peaks above 300 °C.

The proposed mechanism of formation of bimetallic Pd-Sn nanoparticles on the surface of  $\gamma$ -Al<sub>2</sub>O<sub>3</sub> based on acetylacetonate precursors.

An issue in the nanoparticles preparation procedure is to seek a method that allows exposing the maximum active sites to the reagents. For metallic supported nanoparticles, the goal is to disperse as much as possible the metallic active phase over the support (SiO<sub>2</sub>, Al<sub>2</sub>O<sub>3</sub>), in order to maximize the surface density of the active sites and the surface-sensitive performance. The literature reports several preparation methods to achieve this desired metal dispersion. Precipitation, coprecipitation and wet-impregnation are the preparation methods most frequently mentioned. The last one, wet-impregnation, has a simple procedure and gives a better way of controlling metal dispersion by the manipulation of experimental process variables, for this reason it has been chosen for the preparation of the samples in this work. Generally, the preparation method of supported nanoparticles is one of the fundamental factors that play an important role in the precursor structure of nanoparticles. Nowadays, the impregnation method is frequently used for preparing supported nanoparticles, including co-impregnation and sequential impregnation. In

order for bimetallic nanoparticles to be effective, the two metals must be in close contact. However, the most common way to make these nanoparticles, a process termed co-impregnation, is unable to do this effectively. During co-impregnation, metal nanoparticles are deposited on the surface of a substrate [85,86]. Many studies have been carried out to investigate the formation of bimetallic Pd-M/Al<sub>2</sub>O<sub>3</sub> (where M-Cu, Pt, Mn) systems obtained by adsorption from non-aqueous solutions (toluene) of acetylacetonate metal complexes. In particular, monometallic Pd and bimetallic Pd-M systems can be prepared by co-impregnating the support with the required amount of dissolved acetylacetonate metal precursors in toluene [73–75,87].

Depending on the activation treatments previously described, one gets nanoparticles having different characteristics. The particle size depends upon the activation treatment. A direct decomposition under argon atmosphere leads to small particles ( $d \approx 5$  nm) [87,88]. A decomposition of the impregnated Pd(acac)<sub>2</sub> precursor under oxygen or hydrogen forms larger particles (15–30 nm) [87,88]. TEM observations clearly show that only the direct decomposition under an argon atmosphere leads to the formation of rather small particles [87,88]. This has been demonstrated on Pd/SiO<sub>2</sub> prepared by impregnation of silica with Pd(acac)<sub>2</sub>, followed by decomposition under Ar flow where the presence of hydrocarbonated residues left on the metal surface are evidenced [26]. Under only Ar treatment can some carbon residues can be left on the surface. Such species disappear after treatment under oxygen flow above 300 °C because organic groups decompose in the temperature range 200–400 °C. After decomposition under oxygen an additional reduction under hydrogen flow at 500 °C has to be required. Previous works have shown that well-dispersed samples are obtained by such a method [73–75]. The same preparation method by diffusional simultaneously impregnation with decomposition, oxidation and reduction treatments could be used to obtain of monometallic Pd and bimetallic Pd-Sn catalysts supported on  $\gamma$ -Al<sub>2</sub>O<sub>3</sub>.

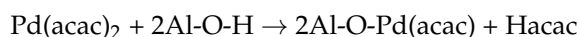
The surface chemistry of  $\gamma$ -Al<sub>2</sub>O<sub>3</sub> aluminum oxide is characterized by the presence of chemical anchoring centers (for example, surface hydroxyl groups), which makes it possible to use the mechanisms of ion exchange with surface functional groups of the support, cation exchange with surface cations included in the structure of the support, ligand exchange/ligand substitution, leading to chemical interaction and fixation of organometallic complexes when deposited from non-aqueous solutions during the preparation of supported bimetallic Pd-M nanoparticles. The adsorption process of acetylacetonate complexes is accompanied by the transformation of their structure. The adsorption of acetylacetonate complexes on the support of the surface during the deposition of organometallic precursors is associated with chemical interactions of the coordination sphere of the metal atom and interaction with the surface of the support by means of various mechanisms. During the preparation of bimetallic Pd-Sn nanoparticles by the co-impregnation method of the  $\gamma$ -Al<sub>2</sub>O<sub>3</sub> support with solutions of Pd(acac)<sub>2</sub> and Sn(acac)<sub>2</sub>Cl<sub>2</sub>, in addition to nonspecific physical adsorption, the precursors interact with coordination unsaturated Al<sup>3+</sup> sites, as well as the interaction with the hydroxyl groups of the support surface  $\gamma$ -Al<sub>2</sub>O<sub>3</sub>. The study of the impregnation of  $\gamma$ -Al<sub>2</sub>O<sub>3</sub> with toluene solutions of acetylacetonates, in particular, Pd(acac)<sub>2</sub>, indicates the presence of chemisorption of the metal chelates due to the reaction with coordination unsaturated Al<sup>3+</sup> centers of the support by the mechanism leading to the formation of surface compounds of acetylacetonate with aluminum of the type [Al(acac)<sub>x</sub>]<sub>s</sub> [89]. We assume that the interaction of a solution of palladium (II) acetylacetonate and tin (IV) bis-acetylacetonate dichloride with the  $\gamma$ -Al<sub>2</sub>O<sub>3</sub> surface will proceed in a similar manner with the formation of surface-adsorbed aluminum acetylacetonate of varying degrees of substitution [Al(acac)<sub>x</sub>]<sub>s</sub>. To explain the features of the observed thermal decomposition, it was assumed that the catalytic action of platinum metal in relation to the decomposition of surface aluminum acetylacetonates [Al(acac)<sub>x</sub>]<sub>s</sub>.



It has been reported that the  $\text{Sn}(\text{acac})_2\text{Cl}_2$  complex reacts with coordination unsaturated  $\text{Al}^{3+}$  ions on the surface of the  $\gamma\text{-Al}_2\text{O}_3$  support [90,91]. It is assumed that the reaction between  $\text{Sn}(\text{acac})_2\text{Cl}_2$  and coordination-unsaturated  $\text{Al}^{3+}$  ions leads to the formation of particles  $[\text{Sn}(\text{acac})^+\text{Cl}_2]_s$  and  $[\text{Al}(\text{acac})]^{2+}_s$  on the  $\gamma\text{-Al}_2\text{O}_3$  surface. In the proposed reaction mechanism, the  $\text{Sn}(\text{acac})_2\text{Cl}_2$  complex gives an acetylacetonate ligand with the formation of a substituted complex  $\text{Sn}(\text{acac})^+\text{Cl}_2$  and surface-adsorbed aluminum acetylacetonate  $\text{Al}(\text{acac})^{2+}_s$ . It is noted that the formation of  $\text{SnCl}_2$  is unlikely, since it is expected that  $\text{Sn}(\text{acac})_2\text{Cl}_2$  will react with  $\text{Al}^{3+}$  to form  $\text{Sn}(\text{acac})^+\text{Cl}_2$  and surface adsorbed aluminum acetylacetonate  $\text{Al}(\text{acac})^{2+}_s$  until the number of coordination unsaturated ions  $\text{Al}^{3+}$  will not be exhausted [90,91].



In addition to the interaction of the coordination sphere of the metal atom with coordination unsaturated  $\text{Al}^{3+}$  ions, the acetylacetonate complex interacts with respect to surface hydroxyl groups of the support  $\gamma\text{-Al}_2\text{O}_3$ , which is associated with specific adsorption by the ion exchange mechanism [85] due to the formation of adsorbed complexes between the electron-deficient chelate parts of the acetylacetonate complex electron-acceptor surface OH groups of the surface of the  $\gamma\text{-Al}_2\text{O}_3$  support.

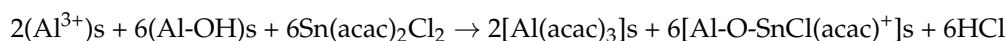
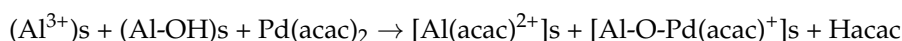


In this case, the character of the interaction of palladium acetylacetonate can be described using the adsorption mechanism with proton exchange. In this interaction, acetylacetonate reacts with one or more hydroxyl (OH) groups on the surface of the oxide support with the release of a free ligand, its transition to an adsorbed state, or followed by mild pyrolysis in an inert argon atmosphere, or removal into the liquid or gas phase. This interaction leads to the formation of covalent oxygen-metal bonds. This type of interaction is typical for reactions occurring during the heat treatment of associatively bound metal acetylacetonates (thermolysis with proton transfer), according to the mechanism:

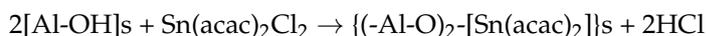


It should be noted that the above mechanisms have a pronounced saturation capacity. In both cases, saturation is associated with a limitation of the number of structural fragments involved in bond formation. For example, the saturation of the interaction with proton exchange is associated with a limited number of hydroxyl groups available on the surface of the oxide support, while the saturation of the interaction by the dissociative adsorption mechanism is associated with a limited number of available coordination unsaturated  $\text{Al}^{3+}$  centers. The saturation by the mechanism of chemical adsorption depends on the specific surface of the support and, generally, is limited. The indicated formal equations do not reflect the full interaction mechanism.

Apparently, from the formally written equations, the above mechanisms are not implemented clearly. The deposition of precursors on the surface of the support leads to the idea of the simultaneous occurrence of several competing mechanisms of adsorption of precursors both with coordination unsaturated  $\text{Al}^{3+}$  centers by the mechanism of chemical adsorption, and with hydroxyl groups of the surface of the support. The overall reaction can be written as follows:



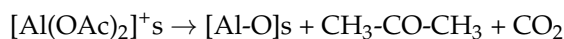
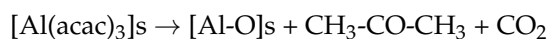
Ligand substitution is also possible with a change in the number of ligands in the internal coordination sphere of the complex by the mechanism of hydrolysis of the metal-ligand bond [92].



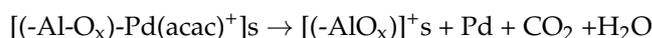
These mechanisms of anchoring of metal complexes can be observed during the deposition of active precursors on surfaces obtained by impregnation from non-aqueous solutions.

The mechanism of formation of  $\text{SnO}_2$  nanoparticles on the surface of  $\gamma\text{-Al}_2\text{O}_3$  is associated with the adsorption of  $[\text{Sn}(\text{acac})_2]^{2+}$  ions on the surface of  $\gamma\text{-Al}_2\text{O}_3$  due to ion exchange between the complex metal ion and the hydrogen ion, which is released from the hydroxyl groups of the  $\gamma\text{-Al}_2\text{O}_3$  support. Part of the released  $\text{H}^+$  is adsorbed on the  $-\text{OH}$  groups forming the  $-\text{OH}_2^+$  group. Electrostatic repulsion between the  $[\text{Sn}(\text{acac})_2]^{2+}$  ion and the  $\text{Al-OH}_2^+$  group prevents further adsorption to achieve adsorption equilibrium.

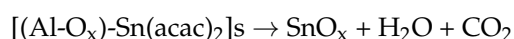
During the heat treatment of samples in an inert argon gas flow at  $500\text{ }^\circ\text{C}$ , the adsorbed particles (adsorbed complexes) decompose on the surface of the  $\gamma\text{-Al}_2\text{O}_3$  support with the formation of acetate, acetone, and chemisorbed oxygen on the aluminum surface  $[\text{Al-O}]$  in accordance with the following reactions, according to [93].



The mechanism of the formation of palladium nanoparticles can be schematically represented in the following form [94].



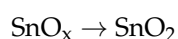
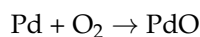
At a temperature  $\approx 300\text{ }^\circ\text{C}$ , the  $\text{Sn}(\text{acac})\text{Cl}^+$  coordination complex on the surface begins to decompose and tin oxide forms [95].



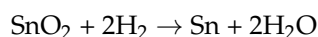
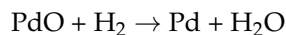
At this step, in the process of subsequent heating, the acetylacetonate ligands of the adsorbed tin complex are oxidized to form  $\text{SnO}_x$  particles strongly dispersed on the  $\gamma\text{-Al}_2\text{O}_3$  surface.

The thermal decompositions of the monometallic Pd and bimetallic Pd-Sn samples are affected by the choice of environment of chemical pretreatments. This step of heat treatment is required for a more complete thermal decomposition of all possible oxidation products of acetylacetonate complexes of metals (such as CO, acetone and acetic acid), residues of amorphous carbon, some of which accumulates due to incomplete oxidation to carbon dioxide and water [96]. We found metallic palladium in the samples after analysis by the XPS method, which may be associated with highly reducing conditions during the decomposition of organic groups in argon. In absence of oxygen in the gaseous phase, the formation of a very stable compound under neutral conditions is favored whereas the oxolation is prevented.

At the next step of heat treatment, the sample is oxidized in an oxygen flow at  $350\text{ }^\circ\text{C}$ , the oxidation of metal nanoparticles of palladium Pd(0) and oxidized nanoparticles of tin on the surface of the  $\gamma\text{-Al}_2\text{O}_3$  support with the formation of nanoparticles of palladium oxide PdO and  $\text{SnO}_2$ , further oxidation of residual amounts of organic compounds to dioxide carbon and water.



At the last step of heat treatment of the sample in a flow of hydrogen at 500 °C, a partial reduction of Pd nanoparticles occurs on the surface of the  $\gamma$ -Al<sub>2</sub>O<sub>3</sub> support of chemisorbed PdO and SnO<sub>2</sub> oxides to the metals Pd and Sn.



Based on the XPS results described above, a formation mechanism of Pd and Sn metallic nanoparticles was supposed and is presented in Figure 6. Three proposed mechanisms in the scheme were distinguished. Here, all chemical reactions are presented schematically. The acetylacetonate complex forms a flat monolayer attached to the surface due to donor-acceptor bonds between the oxygen atoms of the surface hydroxyl groups with the metal ions of the acetylacetonate complex. This allows complex molecules to occupy the most favorable positions from the energetic point of view, i.e., in the surface plane, which causes a significant decrease in the specific surface area and, consequently, the ability of molecules of the acetylacetonate complex to attach to the surface.

The adsorbed complex has two acetylacetonate ligands and, most likely, two additional oxygen ligands from the support. This adsorbed complex is illustrated in the figure (Figure 7a–c). It is the presence of Al in the materials that leads to the ligand exchange reaction and, consequently, to the formation of covalent bonds Pd–O–Al and Sn–O–Al. This can be explained by the acidic nature of the Al–OH groups present in this material. Thus, the deposition of [Pd(acac)<sub>2</sub>] complexes on the surface of the support occurs due to the exchange reaction of the ligands of the acetylacetonate complex with the surface hydroxyl groups of Al–OH. Acetylacetonate ligands are removed in the form of acetylacetone at the first stage of heat treatment in an inert argon atmosphere (pyrolysis) by surface hydroxyl groups Al–OH. Post heat treatment by oxidation or at 350 °C was associated with the removal of the remaining acetylacetonate ligands. It is assumed that the adsorbed layers containing metal ions, with the formation of mixed phases between palladium and tin, due to specific interactions of electron-donor oxygen atoms in the functional groups of the adsorbed complexes of the acceptor metal ions in chelates. Investigation of the steps of thermal decomposition and oxidation-reduction treatments by the XPS method have been carried out.

According to the literature data [78,79,97–101], palladium supported on Al<sub>2</sub>O<sub>3</sub> may exist in three main forms (Pd, PdO and PdO<sub>2</sub>) or their combination. The values of binding energies of the Pd 3d<sub>5/2</sub> XPS peak in these compounds are generally Pd 3d<sub>5/2</sub> = 335.1–335.4 eV for Pd(0) [97–99], Pd 3d<sub>5/2</sub> = 336.8–337.2 eV [97–99] or 336.3–336.8 eV [78,79] for PdO and Pd 3d<sub>5/2</sub> = 337.8–339.3 eV for PdO<sub>2</sub> [100,101]. Larger values of binding energy Pd 3d<sub>5/2</sub> = 338.7 eV can also be attributed to size effects in small particles or clusters; these clusters are epitaxially bound to the support surface and may be covered with an aluminum oxide layer consisting of a palladium–aluminate compound at the palladium–alumina interface boundary [78].

The XPS Pd 3d<sub>5/2</sub>–Pd 3d<sub>3/2</sub> spectra shown in Figure 8 for 1Pd1Sn/ $\gamma$ -Al<sub>2</sub>O<sub>3</sub> sample correspond to three states: after preparation procedure (deposition of the metallic precursors on the  $\gamma$ -Al<sub>2</sub>O<sub>3</sub> surface), after oxidation under O<sub>2</sub> and after reduction under H<sub>2</sub>. These spectra can be decomposed in three contributions with binding energy Pd 3d<sub>5/2</sub> = 335.1 and 336.8 eV, corresponding to palladium in the reduced Pd(0) and oxidized Pd(2+) states in PdO, with a prevalence of the second one; and a contribution with a larger value for the binding energy Pd 3d<sub>5/2</sub> = 338.7 eV which is in perfect agreement with the formation of palladium–aluminate structures [78]. The evolution of the three contributions is consistent with the successive (oxidation and reduction) treatments after preparation.

As shown in Figure 8, the XPS results confirmed that after the complex was fixed on the surface of the  $\gamma$ -Al<sub>2</sub>O<sub>3</sub> support, the maximum of the Pd 3d<sub>5/2</sub> line associated with the chemical state on the support surface remained in the Pd(2+) oxidation state. It is known that the maximum binding energy of Pd 3d<sub>5/2</sub> in the coordination complex Pd(acac)<sub>2</sub> is 338.5 eV, which is consistent with the literature data [102]. The binding energy of the sample containing the adsorbed complex (–AlO<sub>x</sub>)–Pd–(acac) is 336.8 eV which is agree with the

literature data [94]. These Pd 3d<sub>5/2</sub> values are consistent with the literature data for the adsorbed complex (–AlO<sub>x</sub>)–Pd–(acac) [94], but do not correspond to either the initial Pd(acac)<sub>2</sub> coordination complex (338.5 eV) [102] or PdO/Al<sub>2</sub>O<sub>3</sub> (336.2 eV) [78,79]. After, the prepared sample was, containing the adsorbed complex (–AlO<sub>x</sub>)–Pd–(acac), undergoes decomposition at 500 °C for 2 h in an Ar atmosphere to completely remove residual organic compounds [96].

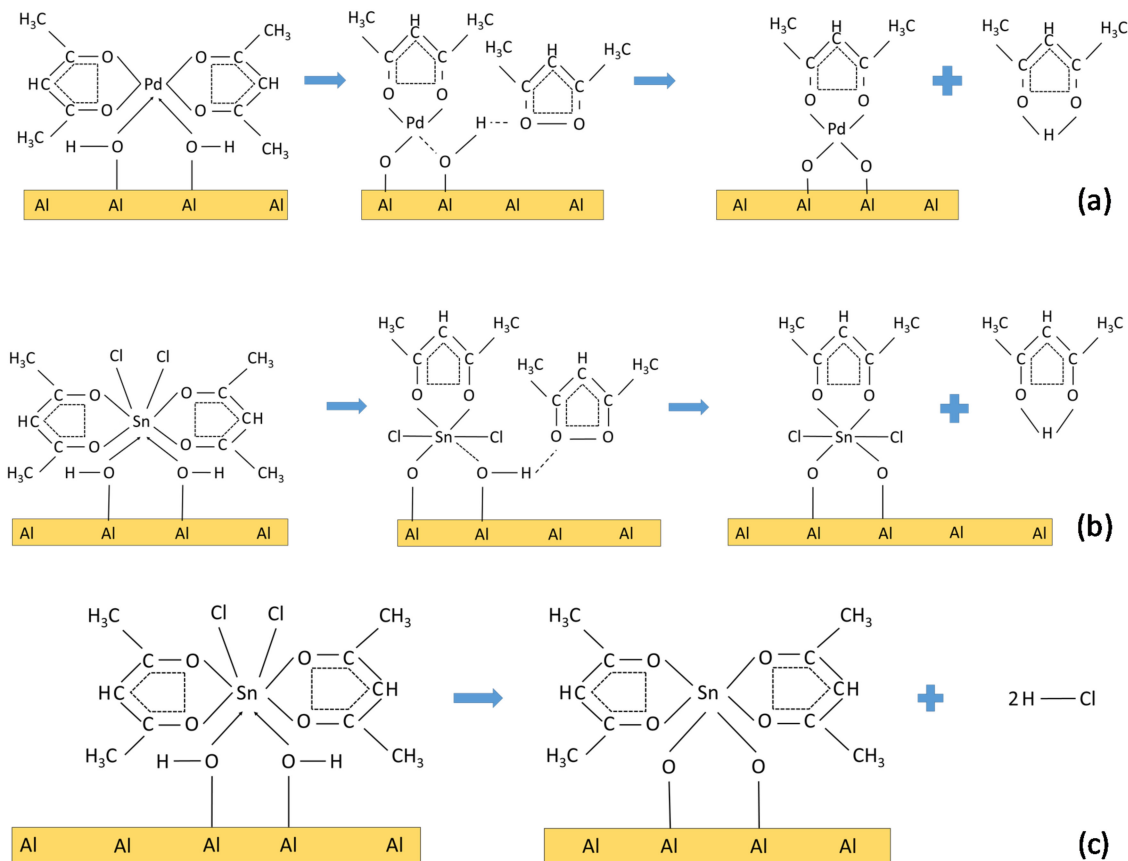


**Figure 7.** (a) The assumed coordination mechanism of Pd(acac)<sub>2</sub> and the structure of the adsorbed palladium complex on the  $\gamma$ -Al<sub>2</sub>O<sub>3</sub> surface. (b) Supposed coordination mechanism of Sn(acac)<sub>2</sub>Cl<sub>2</sub> and the structure of the adsorbed tin complex on the  $\gamma$ -Al<sub>2</sub>O<sub>3</sub> surface. (c) Supposed coordination mechanism of Sn(acac)<sub>2</sub>Cl<sub>2</sub> and the structure of the adsorbed tin complex on the  $\gamma$ -Al<sub>2</sub>O<sub>3</sub> surface by ligand substitution.

After the oxidative pretreatment of the sample in an O<sub>2</sub> atmosphere at 350 °C for 2 h, the XPS spectrum indicates the decomposition of the initial surface-adsorbed complex (–AlO<sub>x</sub>)–Pd–(acac) and its transformation into PdO. A small shift of the binding energy from 336.8 eV to 337.2 eV for 1Pd1Sn/ $\gamma$ -Al<sub>2</sub>O<sub>3</sub> sample after the pretreatment in an O<sub>2</sub> atmosphere at 350 °C for 2 h may indicate the formation of PdO particles. The maximum binding energy of Pd 3d<sub>5/2</sub>, which corresponds to PdO, is at a level of 337.2 eV, which is consistent with the previous data for PdO [97–99], while the binding energy of the Pd 3d<sub>5/2</sub> for adsorbed complex (–AlO<sub>x</sub>)–Pd–(acac) is centered at 336.8 eV [94]. The value of binding energy Pd 3d<sub>5/2</sub> equals to 337.2 eV and corresponds to the extended phase of the oxide PdO [103,104]. After reduction treatment in H<sub>2</sub> atmosphere at 500 °C for 2 h of the 1Pd1Sn/ $\gamma$ -Al<sub>2</sub>O<sub>3</sub>, the value of binding energy Pd3d<sub>5/2</sub> = 336.3 correspond to palladium in the structure of two-dimensional surface oxide layer PdO [104,105]. After reduction treatment in H<sub>2</sub> atmosphere at 500 °C for 2 h the binding energy of Pd 3d<sub>5/2</sub> for 1Pd1Sn/ $\gamma$ -Al<sub>2</sub>O<sub>3</sub> sample is slightly shifted towards lower binding energy with a maximum at 334.7 eV suggesting that tin addition modifies the electronic properties of Pd and that bimetallic alloy particles are formed. For comparison, the binding energy for palladium metal Pd(0) is at 335.2 eV after the oxidation pretreatment at 350 °C for 2 h in oxidation O<sub>2</sub> atmosphere.

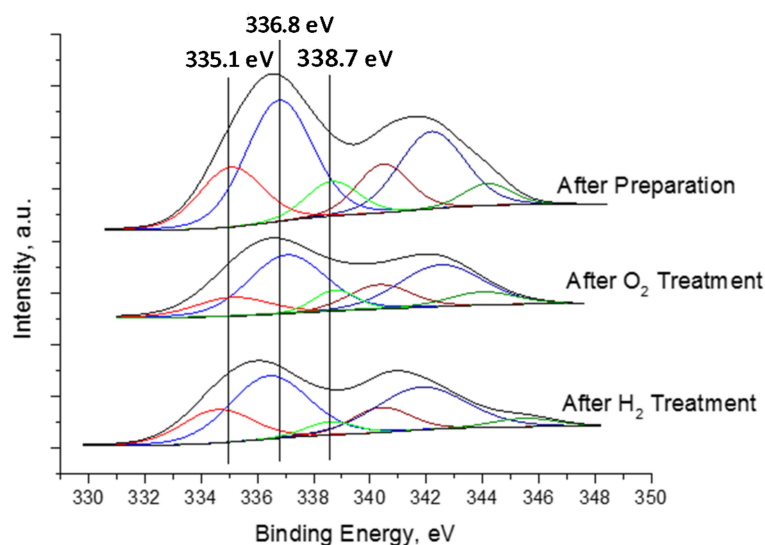


**Figure 8.** XPS spectra of the Pd $3d_{5/2}$  core-level after various steps of heat treatments of the sample 1Pd1Sn/ $\gamma$ -Al $_2$ O $_3$ : after preparation procedure (deposition of the metallic precursors), after oxidative pretreatment in O $_2$  atmosphere at 350 °C for 2 h and after reduction treatment in H $_2$  atmosphere at 500 °C for 2 h.

To better understand the contribution of different states, the XPS spectra of Sn 3d were deconvoluted. In Figure 9 shows the XPS spectra of Sn 3d $_{3/2}$  and the Sn 3d $_{5/2}$  signal that can be decomposed into two symmetrical peaks, as shown in Figure 9. XPS spectra of the Sn 3d $_{5/2}$  after preparation procedure (deposition of the metallic precursors on the  $\gamma$ -Al $_2$ O $_3$  surface) of the 1Pd1Sn/ $\gamma$ -Al $_2$ O $_3$  sample with the lowest binding energy value corresponds to the Sn (0) state, which can be attributed to metallic tin species (Sn 3d $_{5/2}$  = 485.8 eV). The peak with the highest binding energy belongs to oxidized Sn (4+) species [106,107], which could be contained adsorbed tin complex (Sn 3d $_{5/2}$  = 487.6 eV) [97]. After its strong chemisorption Sn(acac) $_2$ Cl $_2$  precursor on the  $\gamma$ -Al $_2$ O $_3$  surface and the oxidation treatment in O $_2$  atmosphere at 350 °C for 2 h of the adsorbed tin complex on the  $\gamma$ -Al $_2$ O $_3$  surface completely oxidizes the residual acac ligands and lead to the formation of the SnO $_2$  species (Sn 3d $_{5/2}$  = 487.7 eV) [108]. The peak position with the binding energy 485.7 eV (Sn 3d $_{5/2}$ ) corresponds to Sn (0) state which can be attributed to the metallic tin species [109,110]. After the reduction in H $_2$  atmosphere at 500 °C for 2 h the peak position with binding energy Sn 3d $_{5/2}$  485.6 eV were ascribed to metallic Sn and the binding energy of Sn 3d $_{5/2}$  (487.3 eV) indicated that Sn was in the Sn(+4) oxidation state in the form SnO $_2$  [109,110]. However, the binding energies of Sn 3d $_{5/2}$  is slightly lower for Sn(4+) oxidation state (487.1 eV) than for oxidized sample (487.6 eV) and for Sn(0) state (485.3 eV) than for oxidized sample (485.7 eV), respectively, which could be assigned to the presence of the bimetallic Pd-Sn species [24,84].

The elemental composition of the surface and near-surface layers (the depth of XPS analysis is tens of angstroms) of the initial monometallic Pd/ $\gamma$ -Al $_2$ O $_3$  sample and bimetallic Pd-Sn samples can be observed from the overview XPS spectrum shown in Figure 10a–c. With the exception of tin lines, lines of basic elements such as aluminum and oxygen, carbon and palladium are found in all the survey spectra presented. Presented also are the atomic fractions (%) of C, Al, O, Pd and Sn, determined from the intensities of the corresponding XPS lines at the core-level (C 1s, Al 2p, O 1s, Pd 3d, Sn 3d) corrected for the atomic sensitivity coefficients (ASF) [97]. It is seen that the carbon content in the samples is in the range of 3–5 at.% and has a maximum for the 1Pd1Sn/ $\gamma$ -Al $_2$ O $_3$  sample (4.85 at.%). As a rule, carbon impurities have a dual origin; it can be introduced both at the stage of sample preparation and as a result of adsorption of hydrocarbons during evacuation of a sample inside an electronic spectrometer. Evaluation of Al chemical states after reduction at 500 °C in H $_2$  are shown in Figure 9. It can be seen that, in full agreement with the quantitative data, the surface Al concentration increases in the following order: Pd/ $\gamma$ -Al $_2$ O $_3$  < 1Pd1Sn/ $\gamma$ -Al $_2$ O $_3$  < 3PdSn/ $\gamma$ -Al $_2$ O $_3$ . The maximum surface concentration

of aluminum is observed for the 3PdSn/ $\gamma$ -Al<sub>2</sub>O<sub>3</sub> sample. This increase in the aluminum content is accompanied by a change in the binding energies of Al 2p, which decreases in the order Pd/ $\gamma$ -Al<sub>2</sub>O<sub>3</sub> > 1Pd1Sn/ $\gamma$ -Al<sub>2</sub>O<sub>3</sub> > 3PdSn/ $\gamma$ -Al<sub>2</sub>O<sub>3</sub>. Despite the difference in binding energies by 1 eV, all the observed features can be attributed to Al<sup>3+</sup> cations bound to oxygen [111], and variations in the binding energy are explained by changes in the coordination of aluminum and/or structural defects.

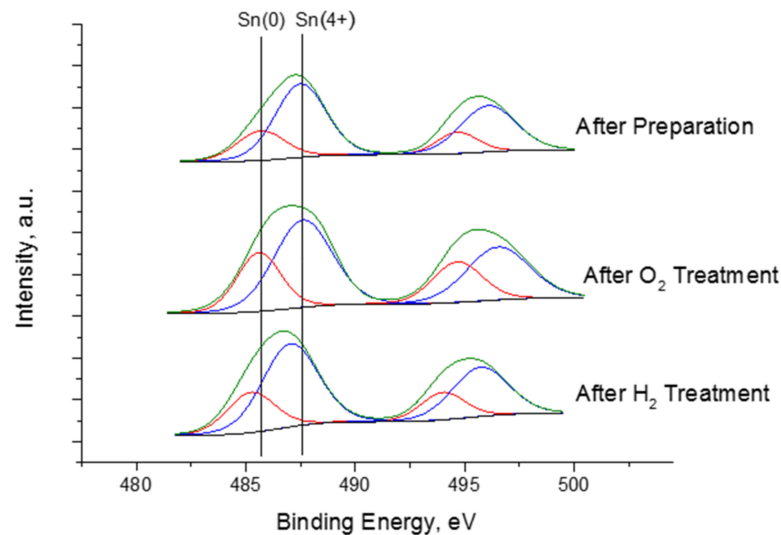
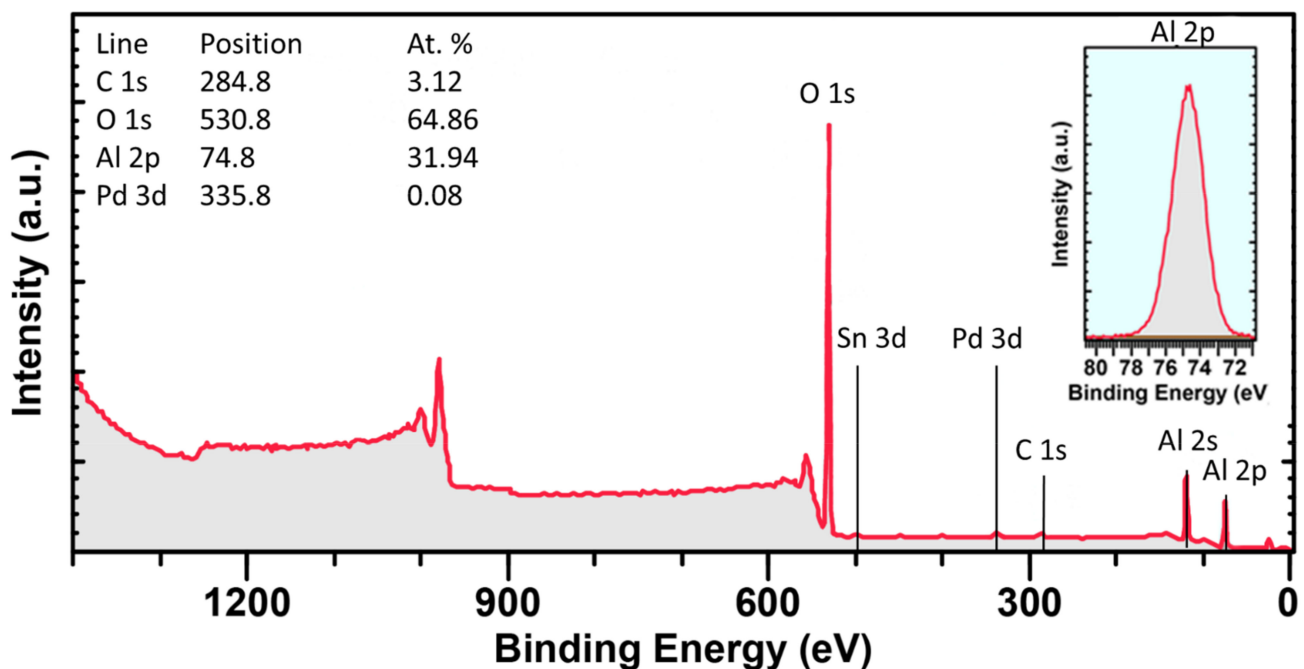
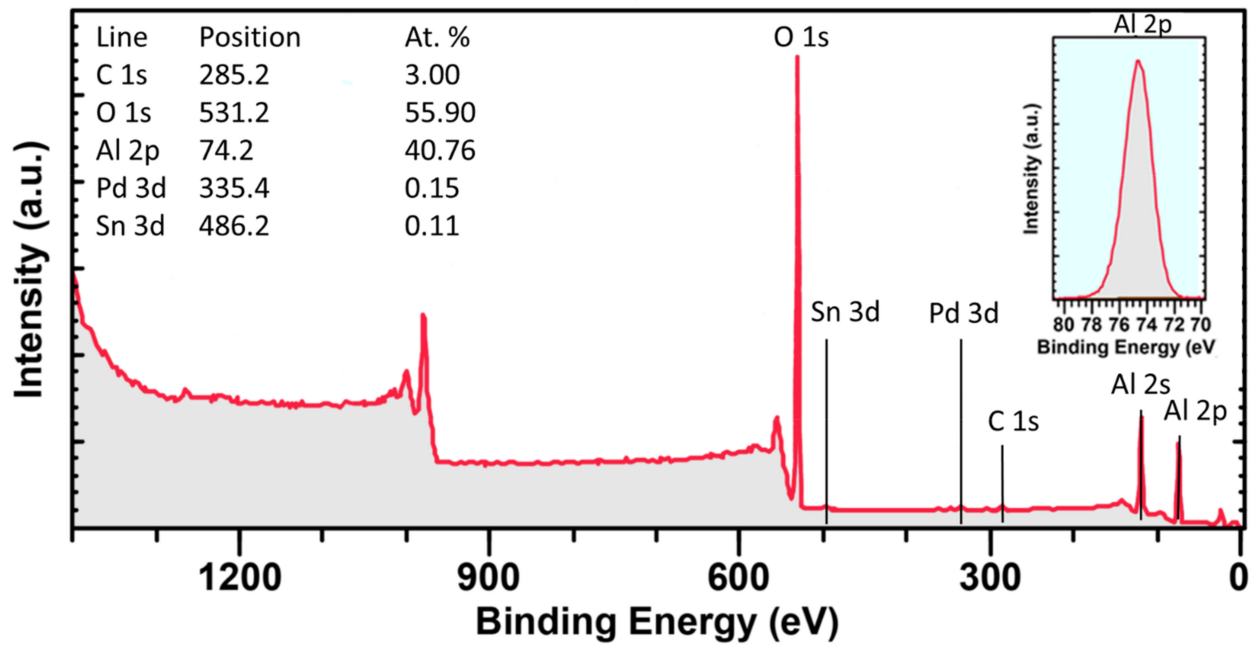


**Figure 9.** XPS spectra of the Sn 3d<sub>5/2</sub> core-level after various steps of heat treatment of the 1Pd1Sn/ $\gamma$ -Al<sub>2</sub>O<sub>3</sub> sample: after preparation procedure (deposition of the metallic precursors), after oxidation treatment in O<sub>2</sub> atmosphere at 350 °C for 2 h and after reduction in H<sub>2</sub> atmosphere at 500 °C for 2 h.

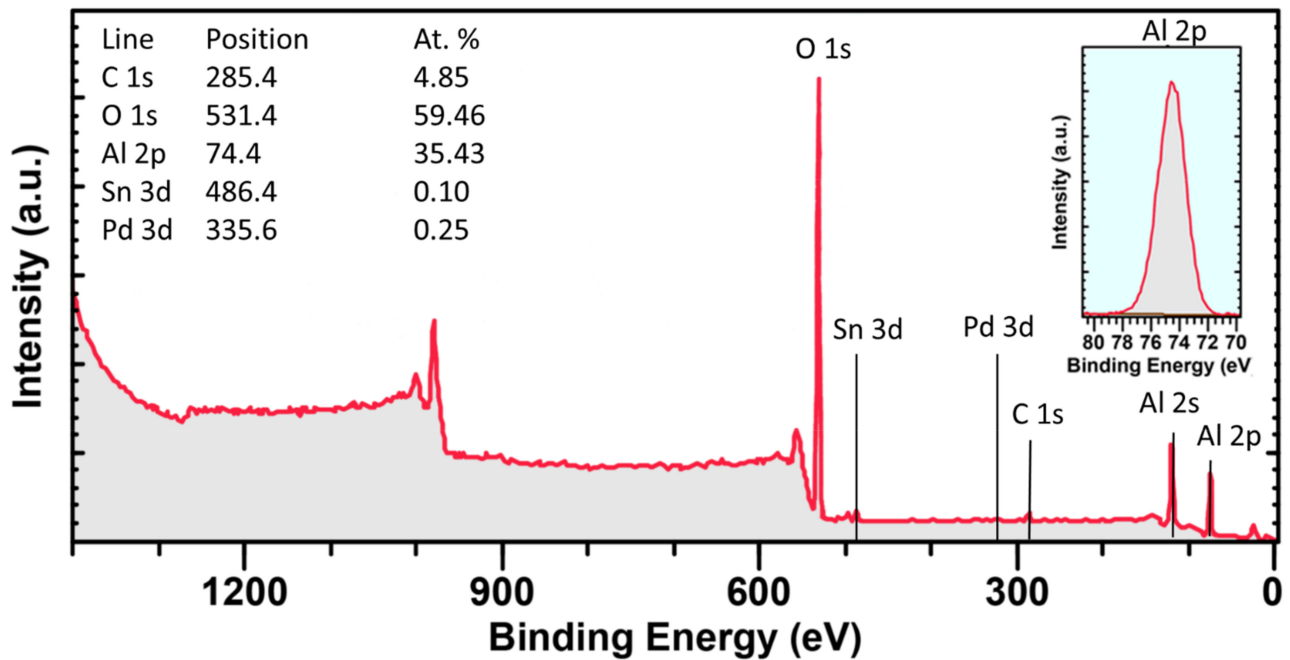


(a)

**Figure 10.** Cont.



(b)



(c)

Figure 10. XPS survey spectra of the samples: (a) Pd/ $\gamma$ -Al<sub>2</sub>O<sub>3</sub>. (b) 3Pd1Sn/ $\gamma$ -Al<sub>2</sub>O<sub>3</sub> and (c) 1Pd1Sn/ $\gamma$ -Al<sub>2</sub>O<sub>3</sub>.

### 3. Materials and Methods

#### 3.1. Preparation of the $\gamma$ -Al<sub>2</sub>O<sub>3</sub> Support and Synthesis of Pd and Bimetallic Pd-Sn Nanoparticles on the $\gamma$ -Al<sub>2</sub>O<sub>3</sub> Surface.

We had chosen a  $\gamma$ -Al<sub>2</sub>O<sub>3</sub> powder composed by 2–5 mm diameter of spheres [112–117]. The alumina balls were crushed in order to get a very fine powder (5.0 g for each one of the three samples). The grinded powder was dried in an evacuated oven at 120 °C for 24 h. It was then sieved and a 0.25–0.5 mm fraction was selected. As starting palladium and tin precursors, organometallic complexes, palladium (II) acetylacetonate (Sigma-Aldrich, St. Louis, MO, USA, 99%) and tin (IV) bis(acetylacetonate) dichloride (Sigma-Aldrich, 98%) were used. Before diffusional impregnation for deposition precursors of the active component, the grinded powder  $\gamma$ -Al<sub>2</sub>O<sub>3</sub> was dried in a vacuum oven at 120 °C for 24 h. The nanoparticles preparation was carried out by diffusional impregnation of the support: pore volume of the  $\gamma$ -Al<sub>2</sub>O<sub>3</sub> was prefilled with using an organic solvent (toluene). For this purpose, the required amount of Pd(acac)<sub>2</sub>, Sn(acac)<sub>2</sub>Cl<sub>2</sub> was dissolved in a large excess of anhydrous toluene (Sigma-Aldrich, 99.8%) with continuous stirring. The approximate volume of toluene that was used for dissolution of metallic precursors is 100 mL. The concentrations of the respective precursors in the resulting solutions are shown in Table 3. To the resulting solution, 5.0 g of support  $\gamma$ -Al<sub>2</sub>O<sub>3</sub> powder was added in the presence of toluene excess for 24 h. The excess solvent was removed on a rotavapor at 80 °C for 30–60 min. Further evaporation of the remaining toluene was carried out in a vacuum oven at 80 °C for 24 h. Finally, thermal and oxidation-reduction treatments were performed and included the following steps: (i) decomposition of the organometallic under Ar (99.998%) at 500 °C for 2 h to minimize the size of the nanoparticles [87,88]; (ii) calcination under O<sub>2</sub> (99.7%) at 350 °C for 2 h to eliminate the organic residues due to the previous decomposition [87,88]; it should be noted that after this treatment the existing nanoparticles were oxidized; (iii) final reduction step under H<sub>2</sub> (99.99%) at 500 °C for 2 h is thus necessary to obtain supported (bi)metallic nanoparticles [87,88]; this was, of course, done after the evacuation of O<sub>2</sub> under Ar for 30 min at 350 °C. The gas flow rate of thermal decomposition, oxidation and reduction treatments is 60 mL/min. All temperature ramps were 1 °C/min. The theoretical calculated content of metals in the samples are given in Table 4. The Pd content has been chosen to be near 1.2 wt%; such a value was sufficient to allow satisfying the physical characterization but not too large in order to obtain a very narrow size distribution of monometallic Pd and bimetallic Pd-Sn nanoparticles on such supports having high specific surface area.

**Table 3.** The theoretical calculated content of metals in synthesized samples.

Name Sample	Atomic Ratio Pd/Sn	m(Pd), mg.	m(Sn), mg.	c (Pd), mmol/L	c (Sn), mmol/L	$\omega$ (Pd), wt%	$\omega$ (Sn), wt%
Pd/ $\gamma$ -Al <sub>2</sub> O <sub>3</sub>	—	60.0	—	5.6	—	1.20	—
3Pd1Sn/ $\gamma$ -Al <sub>2</sub> O <sub>3</sub>	3:1	43.7	16.3	4.1	1.4	0.87	0.33
1Pd1Sn/ $\gamma$ -Al <sub>2</sub> O <sub>3</sub>	1:1	28.4	31.7	2.7	2.7	0.57	0.63

**Table 4.** Specific surface area, total pore volume and average pore size for samples.

Name Sample	Specific Surface Area, m <sup>2</sup> /g	Total Pore Volume, cm <sup>3</sup> /g	Average Pore Size, nm
Pd/ $\gamma$ -Al <sub>2</sub> O <sub>3</sub>	335	0.44	6.0
3Pd1Sn/ $\gamma$ -Al <sub>2</sub> O <sub>3</sub>	282	0.41	5.8
1Pd1Sn/ $\gamma$ -Al <sub>2</sub> O <sub>3</sub>	284	0.42	5.9

#### 3.2. Specific Surface Measurements-BET Method

The specific surface area and pore volume of the samples were determined by N<sub>2</sub> sorption at −196 °C using a TriStar II 3020 analyzer (Micromeritics, Norcross, GA, USA). Prior to the analysis, all samples were outgassed at 200 °C under vacuum for 2 h. The

specific surface area ( $S$ ,  $\text{m}^2/\text{g}$ ) was calculated using the Brunauer-Emmett-Teller (BET) method. The total pore volume ( $V$ ,  $\text{cm}^3/\text{g}$ ) were determined by the Barrett-Joyner-Halenda (BJH) method from the desorption curves of the adsorption isotherms.

### 3.3. Chemical Elemental Analysis-ICP-OES

The composition of samples was determined using an inductively coupled plasma-optical emission spectroscopy (ICP-OES) (Activa, Jobin Yvon, Edison, NJ, USA) Pd was dissolved in a mixture of  $\text{H}_2\text{SO}_4$  + aqua regia at 250–300 °C before analysis. Sn-containing samples were dissolved in a mixture  $\text{H}_2\text{SO}_4$  +  $\text{HNO}_3$  at 250–300 °C then 20% HCl at room temperature.

### 3.4. Electron Microscopy Study and Local Elemental Analysis-TEM-EDX

Transmission electron microscopy (TEM) was used to observe the distribution of the (bi-)metallic nanoparticles over the alumina support and to gain quantitative insight on the characteristics (size distributions, local chemical composition, atomic structure) of the supported catalysts. We used a JEOL JEM 2010 (JEOL Ltd., Tokyo, Japan) transmission electron microscope, operating at 200 kV, equipped with a  $\text{LaB}_6$  thermoionic electron gun, a high-resolution pole piece (0.140 nm information limit) and a Pentafet Link-Isis energy dispersive X-ray (EDX) spectrometer from Oxford Instruments (Abingdon, UK). Prior to observation, analyzed samples were diluted in ethanol, ultrasonicated and dispersed on an electron microscopy Cu grid (3.05 mm, 300 mesh) coated with a holey-carbon film. The general morphology of the samples (dispersion of the (bi-)metallic nanoparticles) together with particle size distributions of Pd and PdSn nanoparticles were obtained from conventional TEM observations; the histograms presented in Figure 1 were obtained by measuring between 300 and 320 nanoparticles for each sample, which, given the narrow distributions and the number of class-sizes chosen (every nm) was largely enough to obtain a relevant statistical information on the samples. The measurements of the size of the nanoparticles were made using the open-source software ImageJ (NIH, Bethesda, MD, USA) and the average diameter was determined in accordance with the classical relation.

$$d = \sum n_i \cdot d_i / \sum n_i$$

where  $n_i$  is the number of particles corresponding to the diameter  $d_i$ , nm.

High resolution images of some nanoparticles were obtained; a selection of these images together with the corresponding 2D-FFTs are presented in Figure 1. We must stress that due to lack of space in the 2D-FFTs, which are small inserts in the HRTEM images, and for clarity reasons we have chosen to designate, in reciprocal space,  $\partial_{(hkl)}$  the corresponding reciprocal distances of the (hkl) spots, instead of the classical  $1/d_{(hkl)}$  designation ( $d_{(hkl)}$  being the interplanar distance for plane (hkl)) which is rather cumbersome to use in such small spaces. The precision on the measurements of the interplanar distances and angles result from both the magnification and the quality of the image, and of course of the size of the nanoparticle also. Indeed, for such small nanoparticles only a limited number of interplanar distances exist and thus the spots in the 2D-FFTs are less well defined than on large nanoparticles or extended films, resulting in inaccuracy of the measurement of the maximum intensity pixel on the reciprocal space spots and thus on the final measure of interplanar distances and angles. The acquisition of the images and their quantitative analysis (2D-FFTs, measurement of interplanar of interplanar distances and angles, etc.) were performed with the software Digital Micrograph (Gatan Instruments, Pleasanton, CA, USA). Finally, the local chemical composition of the nanoparticles was performed by EDX in the TEM. Even though the  $\text{LaB}_6$  thermionic gun of the microscope can achieve rather small probes (down to 5 nm) that in principle allow to perform EDX on individual particles, the electron density in such probes is rather low and so acquisition times required for very small nanoparticles (<5 nm) are very long and inconsistent with the stability of such nanoparticles under a highly focussed beam. We have thus chosen to perform EDX measurements with a 15 nm decondensed probe over collections of 5 to 10 nanoparticles in order to have enough

signal and keep the nanoparticles stable under the beam. Despite these precautions only around 30 (of these very time consuming and delicate) measurements were made for each sample. Nevertheless, we also made three measurements over larger isolated nanoparticles (5 nm) for each sample (see Figure 3b; at% of Pd is given, Sn at% being the complement to 100%, of course) that confirmed the rather good homogeneity of their (local) chemical composition consistent with the global chemical composition obtained by ICP-OES and the local EDX measurements made over 5–10 nanoparticles (Figure 3a).

### 3.5. Surface Analysis-XPS

XPS analysis was performed with a Kratos Axis Ultra DLD spectrometer (Kratos Analytical Ltd., Manchester, UK), equipped with a hemispherical analyzer, and a state-of-the-art delay line detector. A monochromated Al-K $\alpha$  X-ray source with charge neutralization was used. In order to reduce the samples prior to analysis, they were treated under H<sub>2</sub> flow at 500 °C for 2 h in a reaction chamber coupled to the ultra-high vacuum XPS chamber. The samples could then be transferred for XPS analysis without air contact and thus without further possibility of contamination. The Al2p line was taken as an internal standard at 73.4 and 73.6 eV and confirmed by checking the binding energy (BE) of the principal component of the peak-fitted C1s envelope which is arbitrarily assigned the value of 284.6 eV; this component was characteristic of C-C and C-H bonds that were generally present in the samples as contaminant carbon. The precision in BE measurements was  $\pm 0.1$  eV for all samples.

### 3.6. Temperature-Programmed Reduction in H<sub>2</sub>-TPR-H<sub>2</sub>

The reactivity of samples with respect to H<sub>2</sub> was studied by temperature-programmed reduction TPR-H<sub>2</sub> method. TPR-H<sub>2</sub> measurements was carried out on a Micromeritics Chemisorb 2750 automated chemisorption analyzer system attached with ChemiSoft TPx software (Micromeritics, Norcross, GA, USA). Before analysis, the samples were oxidized in O<sub>2</sub> flow at 500 °C for 2 h with temperature ramp 10 °C/min. The sample mass of 100 mg, from  $-50$  °C to 300 °C with temperature ramp 10 °C/min and a carrier gas composed of 10% H<sub>2</sub> in Ar were used. During reduction, a cold trap was placed before the detector to remove water produced. A thermal conductivity detector (TCD) was used to measure the amount of hydrogen consumption.

## 4. Conclusions

In conclusion, we have described a route to the preparation of bimetallic Pd-Sn nanoparticles and characterized their morphology and electronic structure. Bimetallic Pd-Sn nanoparticles supported on  $\gamma$ -Al<sub>2</sub>O<sub>3</sub> were prepared by the diffusional co-impregnation method displayed in this work using Pd(acac)<sub>2</sub> and Sn(acac)<sub>2</sub>Cl<sub>2</sub> as metal precursors because of their higher dispersion of nanoparticles they yield. The prepared samples contained  $\approx 1.3$  wt% of active phase, which indicated that the preparation method was very effective in terms of content of Pd and Sn in the bimetallic samples. The TEM-EDX study also confirms that co-impregnation is an efficient and simple method to produce bimetallic Pd-Sn nanoparticles, supported onto  $\gamma$ -Al<sub>2</sub>O<sub>3</sub>. The results by TEM-EDX show that, for both PdSn samples, the nanoparticles are bimetallic and that the composition is close to the desired one. Morphology analysis of obtained samples by TEM showed for both Pd and bimetallic Pd-Sn samples that the supported nanoparticles have a small size with rather narrow uniform size distribution over the support surface. The results shown for both bimetallic Pd-Sn sample clearly reveal that these individual nanoparticles are bimetallic and establish the validity of the local EDX measurements performed over small collections of nanoparticles. A very large majority of the nanoparticles are bimetallic and consistent with global ICP-OES results. Thermal decomposition of acetylacetonate precursors leads to the formation of bimetallic nanoparticles where the of palladium both Pd(0) species and oxidized PdO species was devised by XPS. Notably, addition of the second element, which is an electron density promoter, leads to a change of the electronic state of the obtained

particles and to the formation of bimetallic species (containing or not oxygen). The addition of Sn conduces to an increased part of PdO of bimetallic Pd-Sn nanoparticles. It may be assumed that addition of Sn during the preparation of supported bimetallic Pd-Sn nanoparticles leads to a competitive reduction reaction of SnO<sub>x</sub> and, possibly, inhibition of the PdO reduction. The TPR-H<sub>2</sub> profiles of the samples show that a new feature is present in the bimetallic samples and the absence of a Pd-β-hydride decomposition feature indicates that there is a strong interaction between the Sn and Pd in these samples. TPR-H<sub>2</sub> shows that Pd and Sn are likely to be mixed to form bimetallic species as the addition of Sn hinders the formation of Pd-β-hydride. The Pd-Sn bimetallic samples showed additional high temperature reduction peaks above 300 °C which are related to Sn reduction.

**Author Contributions:** Conceptualization, F.J.C.S.A. and I.K.; validation, I.B., F.J.C.S.A. and G.M.; investigation, I.B., F.J.C.S.A. and G.M.; resources, F.J.C.S.A., G.M. and I.K.; writing—original draft preparation, I.B.; writing—review and editing, I.B., F.J.C.S.A. and G.M.; visualization, I.B.; supervision, F.J.C.S.A. and I.K.; project administration, I.K.; funding acquisition, I.K. All authors have read and agreed to the published version of the manuscript.

**Funding:** This research was financially supported of The Ministry of Science and Higher Education of Russia (surface analysis by XPS, elemental analysis by ICP-OES and TPR-H<sub>2</sub> experiments) and The National Research Tomsk State University by The Competitiveness Improvement Programme grant (TEM observations).

**Acknowledgments:** The authors accord a thank Aleksandr V. Chernyavskii by Nanocenter, MIREA, Russian Technological University for XPS studies.

**Conflicts of Interest:** The authors declare no conflict of interest.

## References

1. Arora, N.; Thangavelu, K.; Karanikolos, G.N. Bimetallic nanoparticles for antimicrobial applications. *Front. Chem.* **2020**, *8*, 412. [[CrossRef](#)]
2. Huynh, K.-H.; Pham, X.-H.; Kim, J.; Lee, S.H.; Chang, H.; Rho, W.-Y.; Jun, B.-H. Synthesis, properties, and biological applications of metallic alloy nanoparticles. *Int. J. Mol. Sci.* **2020**, *21*, 5174. [[CrossRef](#)] [[PubMed](#)]
3. Srinoi, P.; Chen, Y.-T.; Vittur, V.; Marquez, M.D.; Lee, T.R. Bimetallic nanoparticles: Enhanced magnetic and optical properties for emerging biological application. *Appl. Sci.* **2018**, *8*, 1106. [[CrossRef](#)]
4. Loza, K.; Heggen, M.; Epple, M. Synthesis, structure, properties, and applications of bimetallic nanoparticles of noble metals. *Adv. Funct. Mater.* **2020**, *30*, 1909260. [[CrossRef](#)]
5. De França Bettencourt, G.M.; Degenhardt, J.; Torres, L.A.Z.; de Andrade Tanobe, V.O.; Soccol, C.R. Green biosynthesis of single and bimetallic nanoparticles of iron and manganese using bacterial auxin complex to act as plant bio-fertilizer. *Biocatal. Agric. Biotechnol.* **2020**, *30*, 101822. [[CrossRef](#)]
6. Boote, B.W.; Byun, H.; Kim, J.H. Silver–gold bimetallic nanoparticles and their applications as optical materials. *J. Nanosci. Nanotechnol.* **2014**, *14*, 1563–1577. [[CrossRef](#)] [[PubMed](#)]
7. Garfinkel, D.A.; Pakeltis, G.; Tang, N.; Ivanov, I.N.; Fowlkes, J.D.; Gilbert, D.A.; Rack, P.D. Optical and magnetic properties of Ag–Ni bimetallic nanoparticles assembled via pulsed laser-induced dewetting. *ACS Omega* **2020**, *5*, 19285–19292. [[CrossRef](#)] [[PubMed](#)]
8. Wang, H.; Guo, J.; Li, J.; Wei, J. Fabrication of bimetallic nanoparticles/multi-walled carbon nanotubes composites for microelectronic circuits. *Carbon* **2011**, *49*, 779–786. [[CrossRef](#)]
9. Chaplin, B.P.; Reinhard, M.; Schneider, W.F.; Schuth, C.; Shapley, J.R.; Strathmann, T.J.; Werth, C.J. Critical review of Pd-based catalytic treatment of priority contaminants in water. *Environ. Sci. Technol.* **2012**, *46*, 3655–3670. [[CrossRef](#)]
10. Ghosh, S.; Roy, S.; Naskar, J.; Kumar Kole, R. Process optimization for biosynthesis of mono and bimetallic alloy nanoparticle catalysts for degradation of dyes in individual and ternary mixture. *Sci. Rep.* **2020**, *10*, 277. [[CrossRef](#)]
11. De, S.; Zhang, J.; Luque, R.; Yan, N. Ni-based bimetallic heterogeneous catalysts for energy and environmental applications. *Energy Environ. Sci.* **2016**, *9*, 3314–3347. [[CrossRef](#)]
12. Gómez, J.C.C.; Moliner, R.; Lázaro, M.J. Palladium-based catalysts as electrodes for direct methanol fuel cells: A last ten years review. *Catalysts* **2016**, *6*, 130. [[CrossRef](#)]
13. Yu, W.; Porosoff, M.D.; Chen, J.G. Review of Pt-based bimetallic catalysis: From model surfaces to supported catalysts. *Chem. Rev.* **2012**, *112*, 5780–5817. [[CrossRef](#)]
14. Zaleska-Medynska, A.; Marchelek, M.; Diak, M.; Grabowska, E. Noble metal-based bimetallic nanoparticles: The effect of the structure on the optical, catalytic and photocatalytic properties. *Adv. Colloid Interface Sci.* **2016**, *229*, 80–107. [[CrossRef](#)]
15. Zhang, W.; Lu, X. Morphology control of bimetallic nanostructures for electrochemical catalysts. *Nanotechnol. Rev.* **2013**, *2*, 487–514. [[CrossRef](#)]

16. Shin, E.W.; Choi, C.H.; Chang, K.S.; Na, Y.H.; Moon, S.H. Properties of Si-modified Pd catalyst for selective hydrogenation of acetylene. *Catal. Today* **1998**, *44*, 137–143. [[CrossRef](#)]
17. Kim, W.J.; Shin, E.W.; Kang, J.H.; Moon, S.H. Performance of Si-modified Pd catalyst in acetylene hydrogenation: Catalyst deactivation behavior. *Appl. Catal. A Gen.* **2003**, *251*, 305–313. [[CrossRef](#)]
18. Santos Aires, F.J.C.; Cervantes, G.G.; Bertolini, J.C. Surface modification of Pd/ $\alpha$ -Si<sub>3</sub>N<sub>4</sub> catalysts through the solvent used during synthesis. Implications on the CO chemisorption properties and catalytic performances. *Catal. Lett.* **2009**, *129*, 266–272. [[CrossRef](#)]
19. Rousset, J.L.; Stievano, L.; Santos Aires, F.J.C.; Geantet, C.; Renouprez, A.J.; Pellarin, M. Hydrogenation of tetralin in the presence of sulfur over  $\gamma$ -Al<sub>2</sub>O<sub>3</sub> supported Pt, Pd and Pd-Pt model catalysts. *J. Catal.* **2001**, *202*, 163–168. [[CrossRef](#)]
20. Maroun, F.; Ozanam, F.; Magnussen, O.M.; Behm, R.J. The role of atomic ensembles in the reactivity of bimetallic electrocatalysts. *Science* **2001**, *293*, 1811–1814. [[CrossRef](#)] [[PubMed](#)]
21. Prinz, J.; Gaspari, R.; Stockl, Q.S.; Gille, P.; Armbruster, M.; Brune, H.; Groning, O.; Pignedoli, C.A.; Passerone, D.; Widmer, R. Ensemble effect evidenced by CO adsorption on the 3-Fold PdGa surfaces. *J. Phys. Chem. C* **2014**, *118*, 12260–12265. [[CrossRef](#)]
22. Dupont, C.; Loffreda, D.; Delbecq, F.; Erhet, E.; Cadete Santos Aires, F.J.; Jugnet, Y. A high pressure PM-IRRAS study of CO and O<sub>2</sub> coadsorption and reactivity on PtSn alloy surfaces. *J. Phys. Chem. C* **2008**, *112*, 10862–10867. [[CrossRef](#)]
23. Jugnet, Y.; Loffreda, D.; Dupont, C.; Delbecq, F.; Erhet, E.; Santos Aires, F.J.C.; Mun, B.S.; Akgul, F.A.; Liu, Z. Promoter effect of early stage grown surface oxides: A near ambient pressure XPS study of CO oxidation on PtSn bimetallics. *J. Phys. Chem. Lett.* **2012**, *3*, 3707–3714. [[CrossRef](#)] [[PubMed](#)]
24. Pattamakomsan, K.; Santos Aires, F.J.C.; Suriye, K.; Panpranot, J. Effects of impregnation solvent and reduction temperature on the catalytic performance of Pd/Al<sub>2</sub>O<sub>3</sub> in the selective hydrogenation of 1,3-butadiene. *React. Kinet. Mech. Catal.* **2011**, *103*, 405–417. [[CrossRef](#)]
25. Berthet, A.; Thomann, A.L.; Santos Aires, F.J.C.; Brun, M.; Deranlot, C.; Bertolini, J.C.; Rozenbaum, J.P.; Brault, P.; Andreatza, P. Comparison of Pd/(bulk SiC) catalysts prepared by atomic beam deposition and plasma sputtering deposition: Characterization and catalytic properties. *J. Catal.* **2000**, *190*, 49–59. [[CrossRef](#)]
26. Cervantes, G.G.; Santos Aires, F.J.C.; Bertolini, J.C. Compared properties of Pd on thermo-conductor supports (SiC, Si<sub>3</sub>N<sub>4</sub>) and Pd on oxide supports (Al<sub>2</sub>O<sub>3</sub>, SiO<sub>2</sub>) for the 1,3-butadiene hydrogenation reaction. *J. Catal.* **2003**, *214*, 26–32. [[CrossRef](#)]
27. Santos Aires, F.J.C.; Ramirez, S.; Cervantes, G.G.; Rogemond, E.; Bertolini, J.C. Application of Pd/ $\alpha$ -Si<sub>3</sub>N<sub>4</sub> catalysts to radiant panels using methane catalytic combustion to obtain infrared emission. *Appl. Catal. A Gen.* **2003**, *238*, 289–301. [[CrossRef](#)]
28. Kurzina, I.; Santos Aires, F.J.C.; Bergeret, G.; Bertolini, J.C. Total oxidation of methane over Pd catalysts supported on silicon nitride. Influence of support nature. *Chem. Eng. J.* **2005**, *107*, 45–53. [[CrossRef](#)]
29. Santos Aires, F.J.C.; Kurzina, I.; Cervantes, G.G.; Bertolini, J.C. Pd catalysts supported on silicon nitride for the combustion of methane: Influence of the crystalline phase, the amorphous fraction and the preparation method on the catalytic properties. *Catal. Today* **2006**, *117*, 518–524. [[CrossRef](#)]
30. Wang, J.; Chen, H.; Hu, Z.; Yao, M.; Li, Y. A review on the Pd-based three-way catalyst. *Catal. Rev. Sci. Eng.* **2015**, *57*, 79–144. [[CrossRef](#)]
31. Silva, T.R.; de Oliveira, D.C.; Pal, T.; Domingos, J.B. The catalytic evaluation of bimetallic Pd-based nanocatalysts supported on ion exchange resin in nitro and alkyne reduction reactions. *New J. Chem.* **2019**, *43*, 7083–7092. [[CrossRef](#)]
32. Biffis, A.; Centomo, P.; Del Zotto, A.; Zecca, M. Pd metal catalysts for cross-couplings and related reactions in the 21st century: A critical review. *Chem. Rev.* **2018**, *118*, 2249–2295. [[CrossRef](#)]
33. Martin, R.; Buchwald, S.L. Palladium-catalyzed Suzuki-Miyaura cross-coupling reactions employing dialkylbiaryl phosphine ligands. *Acc. Chem. Res.* **2008**, *41*, 1461–1473. [[CrossRef](#)] [[PubMed](#)]
34. Pattamakomsan, K.; Ehret, E.; Morfin, F.; Gélín, P.; Jugnet, Y.; Prakash, S.; Bertolini, J.C.; Panpranot, J.; Santos Aires, F.J.C. Selective hydrogenation of 1,3-butadiene over Pd and Pd<sub>3</sub>Sn catalysts supported on different phases of alumina. *Catal. Today* **2011**, *164*, 28–33. [[CrossRef](#)]
35. Nemsak, S.; Masek, K.; Matolin, V. RHEED and XPS study of Pd–Sn bimetallic system growth. *Surf. Sci.* **2007**, *601*, 4475–4478. [[CrossRef](#)]
36. Skala, T.; Veltruska, K.; Sedlacek, L.; Masek, K.; Matolinova, I.; Matolin, V. Photoelectron-spectroscopic and reactivity investigation of thin Pd–Sn films prepared by magnetron sputtering. *Appl. Surf. Sci.* **2007**, *253*, 5400–5403. [[CrossRef](#)]
37. Masek, K.; Mixa, M.; Nemsak, S.; Matolin, V. Study of the growth of supported Pd–Sn bimetallic nanoclusters. *Thin Solid Films* **2006**, *515*, 563–566. [[CrossRef](#)]
38. Tsud, N.; Skala, T.; Sutara, F.; Veltruska, K.; Dudr, V.; Fabik, S.; Sedlacek, L.; Chab, V.; Prince, K.C.; Matolin, V. Electronic properties of Sn/Pd intermetallic compounds on Pd(110). *Surf. Sci.* **2005**, *595*, 138–150. [[CrossRef](#)]
39. Tsud, N.; Johaneck, V.; Stara, I.; Veltruska, K.; Matolin, V. XPS, ISS and TPD study of Pd Sn interactions on Pd–SnOx systems. *Thin Solid Films* **2001**, *391*, 204–208. [[CrossRef](#)]
40. Skala, T.; Veltruska, K.; Moroseac, M.; Matolinova, I.; Cirera, A.; Matolin, V. Redox process of Pd–SnO<sub>2</sub> system. *Surf. Sci.* **2004**, *566–568*, 1217–1221. [[CrossRef](#)]
41. Matolin, V.; Matolinova, I.; Mori, T.; Yoshitake, M. Study of palladium interaction with magnetron sputtered SnO<sub>2</sub> films. *J. Surf. Sci. Nanotech.* **2006**, *4*, 497–503. [[CrossRef](#)]

42. Sales, E.A.; Bugli, G.; Ensueque, A.; Mendes, M.J.; Bozon-Verduraz, F. Palladium catalysts in the selective hydrogenation of hexa-1,5-diene and hexa-1,3-diene in the liquid phase. Effect of tin and silver addition Part 1. Preparation and characterization: From the precursor species to the final phases. *Phys. Chem. Chem. Phys.* **1999**, *1*, 491–498. [[CrossRef](#)]
43. Sales, E.A.; Jove, J.; Mendes, M.J.; Bozon-Verduraz, F. Palladium, Palladium–Tin, and Palladium–Silver Catalysts in the Selective Hydrogenation of Hexadienes: TPR, Mössbauer, and Infrared Studies of Adsorbed CO. *J. Catal.* **2000**, *195*, 88–95. [[CrossRef](#)]
44. Verdier, S.; Didillon, B.; Morin, S.; Jumas, J.C.; Olivier-Fourcade, J.; Uzio, D. Pd–Sn/Al<sub>2</sub>O<sub>3</sub> catalysts from colloidal oxide synthesis: I. Preparation of the catalysts. *J. Catal.* **2003**, *218*, 280–287. [[CrossRef](#)]
45. Garron, A.; Lazar, K.; Epron, F. Effect of the support on tin distribution in Pd–Sn/Al<sub>2</sub>O<sub>3</sub> and Pd–Sn/SiO<sub>2</sub> catalysts for application in water denitration. *Appl. Catal. B Environ.* **2005**, *59*, 57–69. [[CrossRef](#)]
46. Palomares, A.E.; Franch, C.; Corma, A. Nitrates removal from polluted aquifers using (Sn or Cu)/Pd catalysts in a continuous reactor. *Catal. Today* **2010**, *149*, 348–351. [[CrossRef](#)]
47. Pintar, A.; Batista, J.; Musevic, I. Palladium-copper and palladium-tin catalysts in the liquid phase nitrate hydrogenation in a batch-recycle reactor. *Appl. Catal. B Environ.* **2004**, *52*, 49–60. [[CrossRef](#)]
48. Fraga, M.A.; de Souza, E.S.; Villain, F.; Appel, L.G. Addition of La and Sn to alumina-supported Pd catalysts for methane combustion. *Appl. Catal. A Gen.* **2004**, *259*, 57–63. [[CrossRef](#)]
49. Lovon-Quintana, J.J.; Santos, J.B.O.; Lovon, A.S.P.; La-Salvia, N.; Valença, G.P. Low-temperature oxidation of methane on Pd–Sn/ZrO<sub>2</sub> catalysts. *J. Mol. Catal. A Chem.* **2016**, *411*, 117–127. [[CrossRef](#)]
50. Vasilchenko, D.B.; Gulyaev, R.V.; Slavinskaya, E.M.; Stonkus, O.A.; Shubin, Y.V.; Korenev, S.V.; Boronin, A.I. Effect of Pd deposition procedure on activity of Pd/Ce<sub>0.5</sub>Sn<sub>0.5</sub>O<sub>2</sub> catalysts for low-temperature CO oxidation. *Catal. Commun.* **2016**, *73*, 34–38. [[CrossRef](#)]
51. Rao, C.; Peng, C.; Peng, H.; Zhang, L.; Liu, W.; Wang, X.; Zhang, N.; Wu, P. In Situ Embedded Pseudo Pd–Sn Solid Solution in Micropores Silica with Remarkable Catalytic Performance for CO and Propane Oxidation. *ACS Appl. Mater. Interfaces* **2018**, *10*, 9220–9224. [[CrossRef](#)] [[PubMed](#)]
52. Freakley, S.J.; He, Q.; Harrhy, J.H.; Lu, L.; Crole, D.A.; Morgan, D.J.; Ntainjua, E.N.; Edwards, J.K.; Carley, A.F.; Borisevich, A.Y.; et al. Palladium-tin catalysts for the direct synthesis of H<sub>2</sub>O<sub>2</sub> with high selectivity. *Science* **2016**, *351*, 965–968. [[CrossRef](#)] [[PubMed](#)]
53. Vicente, A.; Lafaye, G.; Especel, C.; Marecot, P.; Williams, C.T. The relationship between the structural properties of bimetallic Pd–Sn/SiO<sub>2</sub> catalysts and their performance for selective citral hydrogenation. *J. Catal.* **2011**, *283*, 133–142. [[CrossRef](#)]
54. Johnston, S.K.; Cherkasov, N.; Perez-Barrado, E.; Aho, A.; Murzin, D.Y.; Ibhaddon, A.O.; Francesconi, M.G. Pd<sub>3</sub>Sn nanoparticles on TiO<sub>2</sub> and ZnO supports as catalysts for semi-hydrogenation: Synthesis and catalytic performance. *Appl. Catal. A Gen.* **2017**, *544*, 40–45. [[CrossRef](#)]
55. Lanza, R.; Bersani, M.; Conte, L.; Martucci, A.; Canu, P.; Guglielmi, M.; Mattei, G.; Bello, V.; Centazzo, M.; Rosei, R. Effect of Crystalline Phase and Composition on the Catalytic Properties of PdSn Bimetallic Nanoparticles in the PROX Reaction. *J. Phys. Chem. C* **2014**, *118*, 25392–25402. [[CrossRef](#)]
56. Willis, J.J.; Goodman, E.D.; Wu, L.; Riscoe, A.R.; Martins, P.; Tassone, C.J.; Cargnello, M. Systematic Identification of Promoters for Methane Oxidation Catalysts Using Size- and Composition-Controlled Pd-Based Bimetallic Nanocrystals. *J. Am. Chem. Soc.* **2017**, *139*, 11989–11997. [[CrossRef](#)]
57. Zhang, J.; Shao, Q.; Zhang, Y.; Bai, S.; Feng, Y.; Huang, X. Promoting the Direct H<sub>2</sub>O<sub>2</sub> Generation Catalysis by Using Hollow Pd–Sn Intermetallic Nanoparticles. *Small* **2018**, *14*, 1703990. [[CrossRef](#)]
58. Li, F.; Shao, Q.; Hu, M.; Chen, Y.; Huang, X. Hollow Pd–Sn Nanocrystals for Efficient Direct H<sub>2</sub>O<sub>2</sub> Synthesis: The Critical Role of Sn on Structure Evolution and Catalytic Performance. *ACS Catal.* **2018**, *8*, 3418–3423. [[CrossRef](#)]
59. Liao, F.; Lo, T.W.B.; Tsang, S.C.E. Recent developments in palladium-based bimetallic catalysts. *ChemCatChem* **2015**, *7*, 1998–2014. [[CrossRef](#)]
60. Sharma, G.G.; Kumar, A.; Sharma, S.; Naushad, M.; Dwivedi, R.P.; Alothman, Z.A.; Mola, G.T. Novel development of nanoparticles to bimetallic nanoparticles and their composites: A review. *J. King Saud Univ. Sci.* **2019**, *31*, 257–269. [[CrossRef](#)]
61. Fan, J.; Du, H.; Zhao, Y.; Wang, Q.; Liu, Y.; Li, D.; Feng, J. Recent progress on rational design of bimetallic Pd based catalysts and their advanced catalysis. *ACS Catal.* **2020**, *10*, 13560–13583. [[CrossRef](#)]
62. Fuchs, G.; Treilleux, M.; Aires, F.S.; Cabaud, B.; Mélinon, P.; Hoareau, A. Cluster-beam deposition for high-quality thin films. *Phys. Rev. A* **1989**, *40*, 6128–6129. [[CrossRef](#)]
63. Rousset, J.L.; Cadrot, A.M.; Aires, F.S.; Renouprez, A.; Mélinon, P.; Perez, A.; Pellarin, M.; Vialle, J.L.; Broyer, M. Preparation of bimetallic Pt<sub>n</sub>Pt<sub>m</sub> supported clusters with well defined stoichiometry. *Surf. Rev. Lett.* **1996**, *3*, 1171–1176. [[CrossRef](#)]
64. Rousset, J.L.; Stievano, L.; Santos Aires, F.J.C.; Geantet, C.; Renouprez, A.J.; Pellarin, M. Hydrogenation of toluene over γ-Al<sub>2</sub>O<sub>3</sub> supported Pt, Pd and Pd–Pt model catalysts obtained by laser vaporisation of bulk metals. *J. Catal.* **2001**, *197*, 335–343. [[CrossRef](#)]
65. Mahfouz, R.; Santos Aires, F.J.C.; Brenier, A.; Ehret, E.; Roumie, M.; NSouli, B.; Jacquier, B.; Bertolini, J.C. Elaboration and characterization of bimetallic nanoparticles obtained by laser ablation of Ni<sub>75</sub>Pd<sub>25</sub> and Au<sub>75</sub>Ag<sub>25</sub> targets in water. *J. Nanopart. Res.* **2010**, *12*, 3123–3136. [[CrossRef](#)]
66. Pongthawornsakun, B.; Mekasuwandumrong, O.; Santos Aires, F.J.C.; Buechel, R.; Baiker, A.; Pratsinis, S.; Panpranot, J. Variability of particle configurations achievable by 2-nozzle flame syntheses of the Au–Pd–TiO<sub>2</sub> system and their catalytic behaviors in the selective hydrogenation of acetylene. *Appl. Catal. A Gen.* **2018**, *549*, 1–7. [[CrossRef](#)]

67. Zhang, J.; Wan, L.; Liu, L.; Deng, Y.; Zhong, C.; Hu, W. PdPt bimetallic nanoparticles enabled by shape control with halide ions and their enhanced catalytic activities. *Nanoscale* **2016**, *8*, 3962–3972. [[CrossRef](#)] [[PubMed](#)]
68. Ehret, E.; Beyou, E.; Mamontov, G.V.; Bugrova, T.A.; Prakash, S.; Aouine, M.; Domenichini, B.; Santos Aires, F.J.C. Bimetallic PdAg nanoparticle arrays from monolayer films of diblock copolymer micelles. *Nanoscale* **2015**, *7*, 13239–13248. [[CrossRef](#)] [[PubMed](#)]
69. Yermakov, Y.I. Supported catalysts obtained by interaction of organometallic compounds of transition elements with oxide supports. *Catal. Rev. Sci. Eng.* **1976**, *13*, 77–120. [[CrossRef](#)]
70. Yermakov, Y.I.; Kuuznetsov, B.N. Supported metallic catalysts prepared by decomposition of surface organometallic complexes. *J. Mol. Catal.* **1980**, *9*, 13–40. [[CrossRef](#)]
71. Berdala, J.; Freund, E.; Lynch, J. Genesis of the metallic phase in a highly dispersed catalyst formed from Pt acetylacetonate on alumine. *J. Phys. Colloq.* **1986**, *47*, 265–268. [[CrossRef](#)]
72. Faudon, J.F.; Senoq, F.; Bergeret, G.; Moraweck, B.; Clugnet, G.; Nicot, C.; Renouprez, A. Properties of supported Pd-Ni catalysts prepared by coexchange and by organometallic chemistry. *J. Catal.* **1993**, *144*, 460–471. [[CrossRef](#)]
73. Renouprez, A.; Lebas, K.; Bergeret, G. A new method of direct synthesis of bimetallic phases: Silica supported Pd-Cu catalysts from mixed acetylacetonates. *J. Mol. Catal. A Chem.* **1997**, *120*, 217–225. [[CrossRef](#)]
74. Renouprez, A.J.; Trillat, J.F.; Moraweck, B.; Massardier, J.; Bergeret, G. Pd-Mn silica supported catalysts: 1. formation of the bimetallic particles. *J. Catal.* **1998**, *179*, 390–399. [[CrossRef](#)]
75. Renouprez, A.J.; Malhomme, A.; Massardier, J.; Cattenot, M.; Bergeret, G. Sulphur resistant palladium-platinum catalysts prepared from mixed acetylacetonates. *Stud. Surf. Sci. Catal.* **2000**, *130*, 2579–2584.
76. White, M.G. Uses of polynuclear metal complexes to develop designed dispersions of supported metal oxides. *Catal. Today* **1993**, *18*, 73–109. [[CrossRef](#)]
77. Wong, A.; Liu, Q.; Griffin, S.; Nicholls, A.; Regalbuto, J.R. Synthesis of ultrasmall, homogeneously alloyed, bimetallic nanoparticles on silica supports. *Science* **2017**, *358*, 1427–1430. [[CrossRef](#)]
78. Ivanova, A.S.; Slavinskaya, E.M.; Gulyaev, R.V.; Zaikovskii, V.I.; Stonkus, O.A.; Danilova, I.G.; Plyasova, L.M.; Polukhina, I.A.; Boronin, A.I. Metal-support interactions in Pt/Al<sub>2</sub>O<sub>3</sub> and Pd/Al<sub>2</sub>O<sub>3</sub> catalysts for CO oxidation. *Appl. Catal. B Environ.* **2010**, *97*, 57–71. [[CrossRef](#)]
79. Slavinskaya, E.M.; Stonkus, O.A.; Gulyaev, R.V.; Ivanova, A.S.; Zaikovskii, V.I.; Kuznetsov, P.A.; Boronin, A.I. Structural and chemical states of palladium in Pd/Al<sub>2</sub>O<sub>3</sub> catalysts under self-sustained oscillations in reaction of CO oxidation. *Appl. Catal. A Gen.* **2011**, *401*, 83–97. [[CrossRef](#)]
80. D'Arino, M.; Pinna, F.; Strukul, G. Nitrate and nitrite hydrogenation with Pd and Pt/SnO<sub>2</sub> catalysts: The effect of the support porosity and the role of carbon dioxide in the control of selectivity. *Appl. Catal. B Environ.* **2004**, *53*, 161–168. [[CrossRef](#)]
81. Delage, M.; Didillon, B.; Huiban, Y.; Lynch, J.; Uzio, D. Highly dispersed Pd based catalysts for selective hydrogenation reactions. *Stud. Surf. Sci. Catal.* **2000**, *130*, 1019–1024.
82. Bratan, V.; Munteanu, C.; Hornoiu, C.; Vasile, A.; Papa, F.; State, R.; Preda, S.; Culita, D.; Ionescu, N.I. CO oxidation over Pd supported catalysts—In situ study of the electric and catalytic properties. *Appl. Catal. B Environ.* **2017**, *207*, 166–173. [[CrossRef](#)]
83. Fang, X.; Fang, D. Performance of palladium-tin bimetallic catalysts supported on activated carbon for the hydrodechlorination of 4-chlorophenol. *RSC Adv.* **2017**, *7*, 40437–40443. [[CrossRef](#)]
84. Arana, J.; de la Piscina, P.R.; Llorca, J.; Sales, J.; Homs, N.; Fierro, J.L.G. Bimetallic Silica-Supported Catalysts Based on Ni–Sn, Pd–Sn, and Pt–Sn as Materials in the CO Oxidation Reaction. *Chem. Mater.* **1998**, *10*, 1333–1342. [[CrossRef](#)]
85. Pakhomov, N.A. *The Scientific Basis for the Preparation of Catalysts: An Introduction to Theory and Practice (in Russian)*; Publishing Company SB RAS: Novosibirsk, Russia, 2011; pp. 172–196.
86. Pakhomov, N.A.; Buyanov, R.A. Current Trends in the Improvement and Development of Catalyst Preparation Methods. *Kinet. Catal.* **2005**, *46*, 669–683. [[CrossRef](#)]
87. Méthivier, C.; Béguin, B.; Brun, M.; Massardier, J.; Bertolini, J.C. Pd/SiC Catalysts: Characterization and Catalytic Activity for the Methane Total Oxidation. *J. Catal.* **1998**, *173*, 374–382. [[CrossRef](#)]
88. Méthivier, C.; Massardier, J.; Bertolini, J.C. Pd/Si<sub>3</sub>N<sub>4</sub> catalysts: Preparation, characterization and catalytic activity for the methane oxidation. *Appl. Catal. A Gen.* **1999**, *182*, 337–344. [[CrossRef](#)]
89. Womes, M.; Lynch, J.; Bazin, D.; Le Peltier, F.; Morin, S.; Didillon, B. Interaction Between Pt(acac)<sub>2</sub> and Alumina Surfaces Studied by XAS. *Catal. Lett.* **2003**, *85*, 25–31. [[CrossRef](#)]
90. Lee, Y.; George, S.M. Atomic layer etching of Al<sub>2</sub>O<sub>3</sub> using sequential, self-limiting thermal reactions with Sn(acac)<sub>2</sub> and hydrogen fluoride. *ACS Nano* **2015**, *9*, 2061–2070. [[CrossRef](#)] [[PubMed](#)]
91. Lee, Y.; DuMont, J.W.; George, S.M. Mechanism of Thermal Al<sub>2</sub>O<sub>3</sub> Atomic Layer Etching Using Sequential Reactions with Sn(acac)<sub>2</sub> and HF. *Chem. Mater.* **2015**, *27*, 3648–3657. [[CrossRef](#)]
92. Fujishima, M.; Jin, Q.; Yamamoto, H.; Tada, H.; Nolan, M. Tin oxide-surface modified anatase titanium(IV) dioxide with enhanced UV-light photocatalytic activity. *Phys. Chem. Chem. Phys.* **2012**, *14*, 705–711. [[CrossRef](#)] [[PubMed](#)]
93. Van-Veen, J.A.R.; De Jong-Versloot, P.C.; Van Kessel, G.M.M.; Fels, F.J. A thermoanalytic-mass spectrometric study of oxide-supported acetylacetonates. *Thermochim. Acta* **1989**, *152*, 359–370. [[CrossRef](#)]
94. Mouat, A.R.; Whitford, C.L.; Chen, B.-R.; Liu, S.; Perras, F.A.; Pruski, M.; Bedzyk, M.J.; Delferro, M.; Stair, P.C.; Marks, T.J. Synthesis of Supported Pd<sub>0</sub> Nanoparticles from a SingleSite Pd<sup>2+</sup> Surface Complex by Alkene Reduction. *Chem. Mater.* **2018**, *30*, 1032–1044. [[CrossRef](#)]

95. Feng, Y.S.; Zhou, S.M.; Li, Y.; Li, C.C.; Zhang, L.D. Synthesis and characterization of tin oxide nanoparticles dispersed in monolithic mesoporous silica. *Solid State Sci.* **2003**, *5*, 729–733. [[CrossRef](#)]
96. Kurajica, S.; Lozic, I.; Pantaler, M. Thermal decomposition of calcium(II) bis(acetylacetonate) n-hydrate. *Polimeri* **2014**, *35*, 4–9.
97. Moulder, J.F.; Stickle, W.F.; Sobol, P.E.; Bomben, K.D. *Handbook of X-ray Photoelectron Spectroscopy*; Perkin-Elmer Corporation Physical Electronics Division: Eden Prairie, MN, USA, 1992.
98. Brun, M.; Berthet, A.; Bertolini, J.C. XPS, AES and Auger parameter of Pd and PdO. *J. Electron. Spectrosc. Relat. Phenom.* **1999**, *104*, 55–60. [[CrossRef](#)]
99. Briggs, D.; Seah, M.P. *Practical Surface Analysis. Volume 1. Auger and X-ray Photoelectron Spectroscopy*, 2nd ed.; Wiley: Chichester, UK, 1990.
100. Kibis, L.S.; Titkov, A.I.; Stadnichenko, A.I.; Koscheev, S.V.; Boronin, A.I. X-ray photoelectron spectroscopy study of Pd oxidation by RF discharge in oxygen. *Appl. Surf. Sci.* **2009**, *255*, 9248–9254. [[CrossRef](#)]
101. Kibis, L.S.; Stadnichenko, A.I.; Koscheev, S.V.; Zaikovskii, V.I.; Boronin, A.I. Highly Oxidized Palladium Nanoparticles Comprising Pd<sup>4+</sup> Species: Spectroscopic and Structural Aspects, Thermal Stability, and Reactivity. *J. Phys. Chem. C* **2012**, *116*, 19342–19348. [[CrossRef](#)]
102. Mazalov, L.N.; Trubina, S.V.; Kryuchkova, N.A.; Tarasenko, O.A.; Trubin, S.V.; Zharkova, G.I. X-Ray Photoelectron Study of Electron Density Distribution In Palladium(II)  $\beta$ -Diketonate Complexes. *J. Struct. Chem.* **2007**, *48*, 253–261. [[CrossRef](#)]
103. Zemlyanov, D.; Klotzer, B.; Gabasch, H.; Smeltz, A.; Ribeiro, F.H.; Zafeiratos, S.; Teschner, D.; Schnorch, P.; Vass, E.; Havecker, M.; et al. Kinetics of Palladium Oxidation in the mbar Pressure Range: Ambient Pressure XPS Study. *Top Catal.* **2013**, *56*, 885–895. [[CrossRef](#)]
104. Titkov, A.I.; Salanov, A.N.; Koscheev, S.V.; Boronin, A.I. Mechanisms of Pd(110) surface reconstruction and oxidation: XPS, LEED and TDS study. *Surf. Sci.* **2006**, *600*, 4119–4125. [[CrossRef](#)]
105. Lashina, E.A.; Slavinskaya, E.M.; Chumakova, N.A.; Stadnichenko, A.I.; Salanov, A.N.; Chumakov, G.A.; Boronin, A.I. Inverse temperature hysteresis and self-sustained oscillations in CO oxidation over Pd at elevated pressures of reaction mixture: Experiment and mathematical modeling. *Chem. Eng. Sci.* **2020**, *212*, 115312. [[CrossRef](#)]
106. Wang, X.; Fan, W.; Zhang, C.; Chi, M.; Zhu, A.; Zhang, Q.; Liu, Q. Well-dispersed Pd–Sn nanocatalyst anchored on TiO<sub>2</sub> nanosheets with enhanced activity and durability for ethanol electrooxidation. *Electrochim. Acta* **2019**, *320*, 134588. [[CrossRef](#)]
107. Zhou, Y.; Niu, M.; Zhu, S.; Liang, Y.; Cui, Z.; Yang, X. Preparation and electrocatalytic performance of nanoporous Pd/Sn and Pd/Sn–CuO composite catalysts. *Electrochim. Acta* **2019**, *296*, 397–406. [[CrossRef](#)]
108. Nolan, M.; Iwaszuk, A.; Tada, H. Molecular Metal Oxide Cluster-Surface Modified Titanium(IV) Dioxide Photocatalysts. *Aust. J. Chem.* **2012**, *65*, 624–632. [[CrossRef](#)]
109. Liu, M.; Tang, W.; Xu, Y.; Yu, H.; Yin, H.; Zhao, S.; Zhou, S. Pd–SnO<sub>2</sub>/Al<sub>2</sub>O<sub>3</sub> heteroaggregate nanocatalysts for selective hydrogenations of p-nitroacetophenone and p-nitrobenzaldehyde. *Appl. Catal. A Gen.* **2018**, *549*, 273–279. [[CrossRef](#)]
110. Chai, S.; Bai, X.; Li, J.; Liu, C.; Ding, T.; Tian, Y.; Liu, C.; Xian, H.; Mi, W.; Li, X. Effect of phase interaction on catalytic CO oxidation over the SnO<sub>2</sub>/Al<sub>2</sub>O<sub>3</sub> model catalyst. *Appl. Surf. Sci.* **2017**, *402*, 12–20. [[CrossRef](#)]
111. Khassin, A.A.; Yurieva, T.M.; Kaichev, V.V.; Bukhtiyarov, V.I.; Budneva, A.A.; Paukshtis, E.A.; Parmon, V.N. Metal–support interactions in cobalt-aluminum co-precipitated catalysts: XPS and CO adsorption studies. *J. Mol. Catal. A Chem.* **2001**, *175*, 189–204. [[CrossRef](#)]
112. Tanashev, Y.Y.; Moroz, E.M.; Isupova, L.A.; Ivanova, A.S.; Litvak, G.S.; Amosov, Y.I.; Rudina, N.A.; Shmakov, A.N.; Stepanov, A.G.; Kharina, I.V.; et al. Synthesis of aluminum oxides from the products of the rapid thermal decomposition of hydrargillite in a centrifugal flash reactor: I. Physicochemical properties of the products obtained by the centrifugal thermal activation of hydrargillite. *Kinet. Catal.* **2007**, *48*, 153–161. [[CrossRef](#)]
113. Kul'ko, E.V.; Ivanova, A.S.; Kruglyakov, V.Y.; Moroz, E.M.; Shefer, K.I.; Litvak, G.S.; Kryukova, G.N.; Tanashev, Y.Y.; Parmon, V.N. Synthesis of aluminum oxides from the products of the rapid thermal decomposition of hydrargillite in a centrifugal flash reactor: II. Structural and textural properties of aluminum hydroxide and oxide obtained from the product of the centrifugal thermal activation of hydrargillite (CTA product). *Kinet. Catal.* **2007**, *48*, 316–326.
114. Kharina, I.V.; Isupova, L.A.; Litvak, G.S.; Moroz, E.M.; Kryukova, G.N.; Rudina, N.A.; Tanashev, Y.Y.; Parmon, V.N. Synthesis of aluminum oxides from the products of the rapid thermal decomposition of hydrargillite in a centrifugal flash reactor: III. Properties of aluminum hydroxides and oxides obtained via the mild rehydration of the products of the centrifugal thermal activation of hydrargillite. *Kinet. Catal.* **2007**, *48*, 327–335.
115. Danilevich, V.V.; Isupova, L.A.; Kagyrmanova, A.P.; Kharina, I.V.; Zyuzin, D.A.; Noskov, A.S. Highly effective water adsorbents based on aluminum oxide. *Kinet. Catal.* **2012**, *53*, 632–639. [[CrossRef](#)]
116. Zotov, R.A.; Glazyrin, A.A.; Danilevich, V.V.; Kharina, I.V.; Zyuzin, D.A.; Volodin, A.M.; Isupova, L.A. Influence of the temperature of calcination of bayerite-containing aluminum hydroxide pellets on the water vapor adsorption capacity and acid-base properties of alumina. *Kinet. Catal.* **2012**, *53*, 570–576. [[CrossRef](#)]
117. Danilevich, V.V.; Isupova, L.A.; Danilova, I.G.; Zotov, R.A.; Ushakov, V.A. Characteristics optimization of activated alumina desiccants based on product of a centrifugal thermal activation of gibbsite. *Russ. J. Appl. Chem.* **2016**, *89*, 343–353. [[CrossRef](#)]